



Puttur, F. et al. (2019) Pulmonary environmental cues drive group 2 innate lymphoid cell dynamics in mice and humans. *Science Immunology*, 4(36), eaav7638. (doi:[10.1126/sciimmunol.aav7638](https://doi.org/10.1126/sciimmunol.aav7638)).

This is the author's final accepted version.

There may be differences between this version and the published version. You are advised to consult the publisher's version if you wish to cite from it.

<http://eprints.gla.ac.uk/185827/>

Deposited on: 03 May 2019

Enlighten – Research publications by members of the University of Glasgow  
<http://eprints.gla.ac.uk>

1 **Pulmonary environmental cues drive group 2 innate lymphoid cell dynamics in mice**  
2 **and humans**  
3

4 Franz Puttur,<sup>1,6</sup> Laura Denney,<sup>1,6</sup> Lisa G. Gregory,<sup>1</sup> Juho Vuononvirta<sup>1</sup>, Robert Oliver,<sup>1</sup> Lewis  
5 J. Entwistle,<sup>1</sup> Simone A. Walker,<sup>1</sup> Mark B. Headley,<sup>2</sup> Ewan J. McGhee,<sup>3</sup> James E. Pease,<sup>1</sup>  
6 Matthew F. Krummel,<sup>4</sup> Leo M. Carlin,<sup>1,3,5\*</sup> and Clare M. Lloyd<sup>1,\*</sup>

7 <sup>1</sup>Inflammation, Repair & Development, National Heart & Lung Institute, Imperial College  
8 London, London, UK

9 <sup>2</sup>Clinical Research Division, Fred Hutchinson Cancer Research Center, Seattle, WA 98109,  
10 USA

11 <sup>3</sup>Cancer Research UK Beatson Institute, Garscube Estate, Bearsden, Glasgow, UK

12 <sup>4</sup>Department of Pathology, University of California, San Francisco, 513 Parnassus Ave, San  
13 Francisco, California, USA

14 <sup>5</sup>Institute of Cancer Sciences, University of Glasgow, UK

15 <sup>6</sup>These authors contributed equally

16 \*Correspondence: [c.lloyd@imperial.ac.uk](mailto:c.lloyd@imperial.ac.uk) & [l.carlin@beatson.gla.ac.uk](mailto:l.carlin@beatson.gla.ac.uk)

17

## 18 **One Sentence Summary**

19 Collagen-I and CCL8-CCR8 axis control the motility of ILC2 cells in the inflamed lung

20

21

22

23

24

25

26

27

28

29

30

31

32

33

34

35

36

37 **Abstract**

38 Group 2 innate lymphoid cells (ILC2s) are enriched in mucosal tissues (e.g. lung) and respond  
39 to epithelial cell-derived cytokines initiating type-2 inflammation. During inflammation, ILC2  
40 numbers are increased in the lung. However, the mechanisms controlling ILC2 trafficking and  
41 motility within inflamed lungs remain unclear and are crucial for understanding ILC2 function  
42 in pulmonary immunity. Using several approaches, including lung intravital microscopy, we  
43 demonstrate that pulmonary ILC2s are highly-dynamic, exhibit amoeboid-like movement and  
44 aggregate in the lung peribronchial and perivascular spaces. They express distinct chemokine  
45 receptors, including CCR8, and actively home to CCL8 deposits located around the airway  
46 epithelium. Within lung tissue, ILC2s were particularly motile in extracellular matrix-enriched  
47 regions. We show that collagen-I drives ILC2 to dramatically change their morphology by  
48 remodeling their actin cytoskeleton to promote environmental exploration critical for regulating  
49 eosinophilic inflammation. Our study provides previously unappreciated insights into ILC2-  
50 migratory patterns during inflammation and highlights the importance of environmental  
51 guidance cues in the lung in controlling ILC2 dynamics.

52

53

54

## 55 **Introduction**

56 Innate lymphoid cells (ILC), are an emerging family of immune cells that originate from fetal  
57 liver and adult bone marrow (BM) progenitors (1, 2). Prenatally, ILC progenitors occupy  
58 peripheral sites from mid to late stages of fetal development (3), and are detectable in  
59 peripheral tissues by embryonic (E) day 15.5 in the mouse (4). Although ILC derive from  
60 common lymphoid progenitors, they lack specific antigen receptors and lymphoid cell lineage  
61 markers, but display diverse effector functions, analogous to T cells (5, 6). Based on distinct  
62 lineage-determining transcription factors, ILC segregate into three different subsets – ILC1,  
63 ILC2 and ILC3 (7-9). Each ILC subset mirrors a T helper cell subset via the production of T  
64 helper cell signature cytokines- IFN- $\gamma$  (Th1/ILC1), IL-13 (Th2/ILC2) and IL-17 (Th17/ILC3)  
65 which act to combat infection by intracellular pathogens, helminths, and extracellular  
66 pathogens respectively (3). Anatomically, different ILC subsets are resident in particular  
67 barrier and non-barrier sites (3), including the BM, skin, secondary lymphoid organs,  
68 peripheral blood and non-lymphoid tissues. ILC3 are vital for the development of adaptive  
69 immune organs in utero, however after birth thymic ILC3 are replaced by ILC2 suggesting that  
70 these cells play an important role in the thymic microenvironment (10). Among non-lymphoid  
71 tissues, ILC2 are enriched in mucosal sites including the lung and small intestine, where they  
72 contribute to local tissue immunoregulation, repair and homeostasis (11, 12). In the mouse  
73 lung, ILC2 predominate (13), and rapidly expand during the first week of life (14, 15),  
74 populating collagen-rich structures associated with medium-sized blood vessels and airways  
75 (14). In a steady state, long term maintenance of ILC2 in peripheral tissues, including the lung,  
76 is mainly supported by self-renewal of proliferative local tissue resident progenitor populations  
77 (4, 15-18). Recent evidence suggests that ICAM-1 supports ILC2 development and function  
78 during lung inflammation (19). However, in T helper type-2 (Th2) cell induced lung  
79 inflammation, ILC2 exit the BM (19, 20) and concurrently numbers are increased in the blood  
80 and lung (21-24). Human and mouse ILC2 express  $\beta$ 2 integrins and these have been  
81 proposed to be involved in cell trafficking since blocking  $\beta$ 2 integrins results in reduced ILC2

82 numbers in the lung following allergen challenge (22). In addition, recent studies have  
83 identified a distinct pre-ILC2 population originating in the gut that migrates to the lung and  
84 other distal sites giving rise to inflammatory ILC2 (iILC2) that provide protection during worm  
85 infection (15). Within the lung, interaction of ILC2 with other immune cell populations is a  
86 critical factor for shaping type 2 inflammation (25).

87

88 Several factors, including the epithelial cell-derived cytokines IL-33, IL-25 and thymic stromal  
89 lymphopoietin (TSLP), contribute to ILC2 activation and function (26). Upon activation, ILC2  
90 produce cytokines, including IL-4, IL-5, IL-13, colony stimulating factor 2 (CSF2; GM-CSF),  
91 and the epidermal growth factor family member amphiregulin (Areg) (13, 27-29). Lipid  
92 mediators, including the arachidonic acid metabolites leukotriene D4 (LTD<sub>4</sub>), prostaglandin D2  
93 (PGD<sub>2</sub>) (30, 31) and sphingosine 1-phosphate (S1P) (15) serve as potent regulators of ILC2  
94 activation, accumulation and function. In contrast PGE2 and PGI2 suppress ILC2 function,  
95 inhibiting GATA-3, IL-5 and IL-13 expression and decreasing proliferation (32, 33). We have  
96 previously demonstrated that epithelial cell-derived transforming growth factor (TGF)- $\beta$ 1 is  
97 critical for ILC2 activation and significantly enhances airway ILC2 chemoactivity and  
98 movement *in vitro* (34). Thus, ILC2 activation, behaviour and function are regulated by a wide  
99 variety of factors.

100

101 Tissue environments critically control optimal immune responses, coordinating timely and  
102 proportionate recruitment, motility, migration, chemotaxis, positioning, and cell–cell interaction  
103 of leukocytes within inflamed tissues (35). Factors, including lipids, cytokines and homing  
104 receptors (HRs) incorporating chemokine receptors (3) controlling migratory patterns of ILC2  
105 in the bone marrow (BM), spleen, gut, mesenteric lymph nodes (36) and skin (37, 38) have  
106 been identified. Lung ILC2 express high levels of  $\beta$ 1 and  $\beta$ 2 integrins, and use  $\beta$ 2 integrins  
107 selectively to migrate from the BM to the lung after intranasal (i.n.) allergen (*Alternaria*  
108 *alternata*) challenge (39). Organ specific imprinting confers differential gene expression

109 patterns on tissue resident pulmonary ILC2 (40). However, ILC2 motility within the lung during  
110 inflammation remains unstudied, and little is known regarding the signals that might regulate  
111 it. Studies investigating T cell motility in the lung have described a combination of cell-intrinsic  
112 signals and physical guidance cues coupled with biochemical signals provided by the  
113 microenvironment in driving cell movement (41). However, the environmental guidance  
114 signals controlling ILC2 dynamic behaviour in the lung remain poorly defined. Here using IL13-  
115 eGFP mice (28), combined with several imaging approaches, including lung intravital  
116 microscopy, we have documented that ILC2 exhibit amoeboid-like movement in the  
117 peribronchial and perivascular space after IL-33 induced lung inflammation. We identified  
118 specific molecules that communicate between the inflamed pulmonary environment and ILC2,  
119 uncovering the major environmental factors from which ILC2 interpret locomotory cues within  
120 the lung.

121

## 122 **Results**

123

### 124 **The number of ILC2 rapidly increases in the peribronchial / perivascular region after** 125 **rIL-33 treatment.**

126 Under homeostatic conditions, ILC2 exist in relatively low numbers in the lung, but are rapidly  
127 enriched after recombinant IL-33 (rIL-33) or rIL-25 induced inflammation (20-24, 39),  
128 promoting tissue repair during inflammation and regulating immune homeostasis. In this  
129 respect, ILC2 are thought to occupy a specific niche in the lung in keeping with their putative  
130 role as tissue resident sentinel cells (14). However, whether this locational niche is shared  
131 with CD4<sup>+</sup> T cells remains unknown. Using *IL13-eGFP* mice, we investigated ILC2 numbers  
132 in various sites in the lung both at homeostasis and after acute exposure to either the fungal  
133 allergen *Alternaria alternata* (Alt) or rIL-33. **We first quantified GFP<sup>+</sup>CD45<sup>+</sup> cells among live**  
134 **lymphocytes that were either lineage positive versus lineage negative cells (fig. S1A).**  
135 **ILC2 were further defined by pre-gating on live (determined using a fixable live dead**  
136 **dye), GFP<sup>+</sup>CD3<sup>-</sup>NKp46<sup>-</sup> cells that were lineage (TCRβ, TCRγδ, CD5, CD19, CD11b,**

137 **CD11c, FCεR1, GR-1, F4/80, and TER-119) negative cells and co-expressed CD90.2,**  
138 **KLRG-1, CD127 and intracellular cytokine IL-13 (fig. S1B).** As expected, in control mice,  
139 ILC2 were present in very low numbers in the airways, lung tissue and lung draining lymph  
140 nodes (mediastinal lymph node) (Fig. 1, A to C) as well as the blood, bone marrow, spleen,  
141 inguinal and mesenteric lymph nodes (fig. S2). However, during inflammation induced by i.n.  
142 administration of rIL-33 or Alt, ILC2 numbers significantly increased in the bronchoalveolar  
143 lavage fluid BAL (Fig. 1A), lung tissue (Fig. 1B) and the lung draining lymph nodes (Fig. 1C)  
144 as well as after rIL-33 treatment in the blood and bone marrow but not spleen, inguinal and  
145 mesenteric lymph nodes (fig. S2). To confirm that we were not excluding unstimulated ILC2  
146 (IL-13<sup>-</sup>/GFP<sup>-</sup>) in our gating, we additionally re-evaluated ILC2 numbers by gating on CD45<sup>+</sup>lin<sup>-</sup>  
147 NKp46<sup>-</sup>CD3<sup>-</sup> cells and analysed the frequency of GATA-3<sup>+</sup> (a faithful transcription factor to  
148 define all ILC2s) cells (fig. S3A). Here we used balb/c mice instead of IL-13 eGFP mice as the  
149 GFP signal was significantly lost following intra-nuclear staining for GATA-3. Balb/c mice were  
150 challenged with PBS, Alt or rIL-33 and lungs, BAL and blood ILC2s were evaluated by gating  
151 on GATA-3<sup>+</sup> ILC2s. Our data suggests that ILC2s in mock treated mice are still very low in  
152 frequency compared to Alt and rIL-33 treatment (fig. S3B and C) and expressed significantly  
153 lower IL-13 and IL-5 (fig. S3D). Furthermore, by phenotyping GATA-3<sup>+</sup> ILC2s for extracellular  
154 markers, our data suggests that each of the surface markers is altered as per the type of  
155 treatment as shown by the percent expression of each marker (fig. S3E-H) further highlighting  
156 the plasticity of ILC2s in inflammation.

157

158 Similarly, imaging precision cut lung slices (PCLS) from rIL-33 treated IL13-eGFP mice,  
159 revealed substantially more IL-13<sup>+</sup>GFP<sup>+</sup> cells (fig. S4A) which largely accumulated around  
160 large airways and large blood vessels and to a lesser extent around alveolar capillaries (fig.  
161 S4B). To establish that the IL-13<sup>+</sup>GFP<sup>+</sup> cells observed after rIL-33 treatment were pre-  
162 dominantly ILC2, we evaluated the proportion of GFP<sup>+</sup> cells that were CD45<sup>+</sup>lin<sup>neg</sup>CD4<sup>-</sup> and  
163 expressed ILC2 defining markers (CD90.2, CD127, KLRG1, CD25 and co-expressed  
164 intracellular IL-13). Our data showed that 98.86% of observed GFP<sup>+</sup> cells were ILC2, and only



165 1.14% of GFP<sup>+</sup> cells were CD4<sup>+</sup> T cells (fig. S4C). The source of IL-13 by ILC2 versus CD4<sup>+</sup> T  
166 cells after 1 week of rIL-33 administration was further quantified (fig. S4D).  
167 Since a minor proportion of CD4<sup>+</sup> T cells produced IL-13 in our lung inflammation model, we  
168 included a CD4-T cell antibody to precisely evaluate the effects of rIL-33 administration on  
169 numbers and phenotype of CD4<sup>-</sup>GFP<sup>+</sup> ILC2 in PCLS studies. Our PCLS imaging revealed that  
170 rIL-33 treatment induced a significant increase in GFP<sup>+</sup> ILC2 numbers compared to Alt or mock  
171 treated mice (Fig. 1D). rIL-33 treatment induced a 6-fold greater ILC2 number compared to Alt  
172 treatment (Fig. 1,D and E), consistent with the number of ILC2 detected by flow cytometry  
173 (Fig. 1, A to C) and with a shared locational distribution in the inflamed lung tissue (fig. S4A).  
174 Interestingly GFP<sup>+</sup> cells surrounding the bronchioles were significantly greater than the GFP<sup>+</sup>  
175 cells in the alveolar tissue (fig. S4B). The majority of the GFP<sup>+</sup> cells were IL-13 producing ILC2  
176 (fig. S4, C and D) and hence represented IL-13<sup>+</sup> activated ILC2, referred from here on as ILC2  
177 for simplicity. Higher magnification views of the peribronchial space bordering the airways  
178 revealed an intimate association of some ILC2 with the airway epithelium and that ILC2 shared  
179 a locational niche with CD4<sup>+</sup> T cells (Fig. 1F, depicting two representative images from a lung  
180 slice). Overall, we demonstrate that rIL-33 treatment significantly increased the number of lung  
181 ILC2 compared to Alt or PBS treatment and ILC2 accumulate around the airways of inflamed  
182 lungs.

183

#### 184 **IL-33 stimulation induces ILC2 motility around blood vessels and airways.**

185 Intranasal administration of either rIL-33 or Alt induces robust inflammation in the lung (42,  
186 43). A hallmark of acute tissue inflammation is leukocyte recruitment. ILC2 are relatively rare  
187 in the lung compared to other leukocytes under homeostatic conditions but accumulate rapidly  
188 after rIL-33 induced inflammation (Fig. 1). We have previously demonstrated that the epithelial  
189 cell derived TGF- $\beta$  induced after rIL-33 treatment promoted a high degree of ILC2 motility *in*  
190 *vitro* (34).

191

192 However, to date, dynamic movement of ILC2 has not been visualized in the lung. Since lung  
193 ILC2 are relatively rare at homeostasis (Fig. 1, B, D and E, fig. S3), we evaluated ILC2  
194 movement in the inflamed lungs of *IL13-eGFP* mice. Imaging live PCLS from rIL-33 treated  
195 *IL13-eGFP* mice showed that ILC2 were motile in the peribronchial and perivascular space  
196 (Fig. 2A; movie S1). Closer examination of the lung tissue surrounding the blood vessel  
197 revealed that the majority of ILC2 exhibited ‘amoeboid-like’ exploratory movement (Fig. 2, B  
198 and C; movies S2 and S3A) with pseudopodia and bleb-like processes in the extravascular  
199 lung tissue surrounding the blood vessel, while a lesser proportion of ILC2 exhibited  
200 ‘oscillatory’ blebbing activity with little actual movement away from their start position (Fig. 2,  
201 B and C; movies S2 and S3B). Similar to oscillatory ILC2, CD4<sup>+</sup> T cells (cyan) did not appear  
202 to displace from their point of origin in the lung tissue (Fig. 2B; movie S2). Cell tracking of ILC2  
203 and CD4<sup>+</sup> T cells (Fig. 2, D and E) revealed that in PCLS from rIL-33-treated mice, ILC2 track  
204 speed (Fig. 2F), track length (Fig. 2G) and track displacement (Fig. 2H) was significantly  
205 higher than that of CD4<sup>+</sup> T cells. Interestingly, ILC2 from Alt treated mouse lungs moved more  
206 slowly, with shorter tracks, compared to rIL-33-treated mice (Fig. 3, A and B). In addition, rIL-  
207 33 treatment induced increased ILC2 track speed (Fig. 3C), track length (Fig. 3D) and track  
208 displacement (Fig. 3 E) compared to Alt treatment. Since rIL33 promoted greater ILC2  
209 movement than Alt treatment, we focused on rIL-33 induced changes on ILC2 motility  
210 thereafter. Since PCLS do not recapitulate the forces exerted by blood-flow and breathing *in*  
211 *vivo*, we also performed lung intravital microscopy in live mice using a similar strategy to  
212 previous work (44). We found that consistent with our data in live PCLS (Fig. 1, D to F, Fig. 2,  
213 A and B), ILC2 were enriched in the extravascular tissue close to larger blood vessels and  
214 exhibited amoeboid-like movement within the lung tissue (Fig. 3F, movie S4A and 4B).

215

216 In summary, our results demonstrate that ILC2s are highly dynamic in the lung after treatment  
217 with either rIL-33 or allergen, where they exhibit amoeboid-like movement and travel faster  
218 over greater distances than CD4<sup>+</sup> T cells.

219

220 **ILC2s utilize distinct chemotactic pathways to home to inflammatory sites in the lung.**

221 We have shown that within the lung, ILC2s display a specific distribution pattern and  
222 movement behaviour distinct from T cells. However, the factors that regulate ILC2 dynamics  
223 are not well understood. Since ILC subsets have key features analogous to T cell populations,  
224 it has been suggested that molecular pathways which control motility, migration and tissue  
225 homing are common to ILC subsets and T cells, but this has not yet been proven. Therefore,  
226 we examined the pattern of chemokine receptor expression on ILC populations (defined as  
227 CD45<sup>+</sup>GFP<sup>+</sup>Lin<sup>neg</sup>KLRG1<sup>+</sup>CD127<sup>+</sup>CD25<sup>var</sup>) isolated from the lungs of rIL-33 treated mice (or  
228 PBS treated controls) (fig. S5A and B). Surprisingly, despite the high degree of resemblance  
229 between ILCs and T cells, many of the prototypic chemokine receptors found on T cell subsets  
230 were absent on ILC, including CCR3, CCR4 (Th2), CCR6 (Th17), and CCR5 and CXCR3  
231 (Th1). Notably, ILC did express both CCR1 and CCR8, which are associated with type 2  
232 cytokine production by T cells in allergic contexts (45).

233

234 Therefore, we examined expression of CCR1, 4 and 8 specifically on IL-13<sup>+</sup> ILC2, finding that  
235 the majority of IL-13<sup>+</sup> ILC2 express CCR1 (>50%) and/or CCR8 (>90%) and that the  
236 expression of these chemokine receptors was higher in rIL-33 treated mice than in PBS  
237 treated controls (Fig. 4A). In contrast to T cells, we found that CCR4 expression was not  
238 associated with a type 2 phenotype in ILC with only 10% of IL-13<sup>+</sup> ILC also expressing CCR4.  
239 Furthermore, *in vivo* activation of ILC2 with rIL-33 did not alter CCR4 expression (Fig. 4A).  
240 Interestingly, we also found significantly greater levels of CCL8 protein, a ligand for CCR8 in  
241 mice (46) in the airways (Fig. 4B) and lungs (Fig. 4C) of rIL-33 treated mice compared to PBS  
242 treated control mice. We additionally evaluated other CCR8 ligands (CCL1) and CCR1 ligands  
243 (RANTES) (fig. S5C and D) in lungs of mice exposed to rIL-33 compared to control treated  
244 mice. PCLS and intravital imaging demonstrated that ILC2 accumulate in the peribronchial  
245 and perivascular space and are highly motile in rIL-33 treated IL13-eGFP mice (Fig. 2, A to C  
246 and Fig. 3F). Hence, we determined whether we could identify CCL8 chemokine deposits in  
247 areas of ILC2 movement in live PCLS of rIL-33 treated IL13-eGFP mice. CCL8 was strongly

248 expressed in the peribronchial space where ILC2 accumulate after rIL-33 treatment, at  
249 significantly greater levels than basal CCL8 expression in control mice (Fig. 4, D and E) with  
250 airway macrophages being the major producer for CCL8 in our model (fig. S5E).

251

252 To examine the migration of ILC2 to chemotactic agents we sorted human ILC2 from  
253 peripheral blood (CD45<sup>+</sup>, Lin<sup>neg</sup>, CD161<sup>+</sup>, CD127<sup>+</sup>, CRTH2<sup>+</sup> and C-Kit<sup>variable-</sup>) then cultured with  
254 recombinant IL-2, IL-7 and IL-33 for at least 4 weeks (resulting in >99% ILC2). These ILC2s  
255 expressed GATA-3 and IL-13 (fig. S6A) and produced IL-13 (fig. S6B). Among the three  
256 cytokines required for ILC2 maintenance, our results suggest that IL-7 signalling in ILC2 was  
257 critical for their survival, proliferation and cytokine production as demonstrated by viability (fig.  
258 S6C) GATA-3 expression (fig. S6D), Ki67 staining (fig. S6E) and IL-5 production (fig. S6F).  
259 We additionally compared differences in motility between ILC2 starved of IL-2 vs IL-33  
260 compared to ILC2 that received all three cytokines. After 12h of live *ex vivo* imaging ILC2 track  
261 speed (fig. S6G) remained comparable (movie S5A, B and C). ILC2 that were starved of IL-7  
262 could not be included in this set up as absence of IL-7 significantly reduced ILC2 viability (fig.  
263 S6C). Our findings are consistent with the literature and reemphasize the importance of IL-7  
264 signalling being critical for the maintenance of ILC2 and other IL-7R<sup>+</sup> lymphocyte populations  
265 (47).

266

267 The potential of *in vitro* cultured ILC2 to migrate to a known ILC2 chemotactic factor - the  
268 eicosanoid PGD<sub>2</sub> (48), was examined using a modified Boyden chamber chemotaxis assay  
269 (Fig. 4F). As expected, all human ILC2 lines tested migrated to PGD<sub>2</sub> and peak chemotaxis  
270 occurred at a concentration of 100nM PGD<sub>2</sub> consistent with previous studies (48). Since we  
271 found CCL8 in the BAL and CCL8 deposits in the lung of rIL-33 treated mice (Fig. 4, D and  
272 E), we queried whether CCL8 could induce the migration of human ILC2. Using the same  
273 modified Boyden chamber assay, we found that CCL8 also induced human ILC2 chemotaxis  
274 in a dose-dependent manner, peaking at 10nM CCL8 (Fig. 4G). We next compared migration

275 of ILC2 to factors thought to influence ILC2 movement. After determining the optimum  
276 concentrations for each factor, we found that although PGD<sub>2</sub> was the most efficacious inducer  
277 of ILC2 migration, TGF- $\beta$ , IL-33 and CCL8 all promoted comparable levels of migration (Fig.  
278 4H). Taken together, these data identify specific chemokine receptor expression in ILC2 and  
279 show the corresponding ligand availability in areas of ILC2 accumulation. In order to confirm  
280 that CCL8-CCR8 axis plays an important functional role in ILC2 migration in vivo, we  
281 administered a blocking antibody against CCR8 or isotype Ab as a control and simultaneously  
282 treated mice with rIL-33. Our live PCLS data showed that blocking CCR8 significantly reduced  
283 ILC2 accumulation in the peribronchial region compared to control mice (Fig. 4, I and J) and  
284 ILC2 migration was impaired after CCR8 receptor blocking (movie S6, A and B) with shorter  
285 tracks depicted as track overlay between treatments (Fig. 4K) and reduced track length (Fig.  
286 4L), track speed (Fig. 4M) and track displacement (Fig. 4N). Closer analysis of ILC2 from each  
287 of these treatments revealed that significantly less of the ILC2 in rIL-33 treated mice receiving  
288 the anti-CCR8 blocking antibody expressed IL-13<sup>+</sup>IL-5<sup>+</sup> (Fig. 4O) and those cells that did  
289 express the type 2 cytokines had significantly less IL-13 and IL-5 as determined by the mean  
290 fluorescence intensity (MFI) (Fig. 4P-R). Overall, our data suggests that the CCL8/CCR8  
291 pathway plays an essential role in inducing ILC2 accumulation, activation and movement  
292 within the lung during rIL-33 induced inflammation.

293

#### 294 **Extracellular matrix proteins, collagen-I, collagen-IV and fibronectin, promote** 295 **increased ILC2 motility**

296 In addition to chemokines, structural guidance cues such as extra cellular matrix (ECM)  
297 proteins have been shown to facilitate movement of immune cells, including T cells (41). In  
298 chronically inflamed lung tissue, as observed during asthma, aberrant ECM expression from  
299 tissue-remodelling can further influence immune cell activation and survival, thereby altering  
300 inflammatory immune responses (49). Therefore, we next examined whether ECM proteins  
301 influenced ILC2 movement. Fibronectin, collagen-I, III (fibrillar collagens) and collagen-IV  
302 (basement membrane collagen) are located around large airways and blood vessels and are

303 altered during lung inflammation (50). Proteoglycans such as versican and tenascin C are  
304 changed during remodelling in various lung disorders, including asthma and chronic  
305 obstructive pulmonary disease (COPD) (51).

306 Therefore, the influence of collagens-I, -III and -IV, fibronectin, and proteoglycans, versican  
307 and tenascin C, on ILC2 movement was examined in a simplified 2D cell migration assay.  
308 Human ILC2 were cultured on these substrates and cell movement tracked over 12h *in vitro*  
309 by using an automated live cell imaging system using culture media with or without heat-  
310 inactivated fetal bovine serum (FBS) as controls. In contrast to serum-free media, collagen-I,  
311 fibronectin and collagen-IV significantly enhanced dynamics of ILC2, as shown in the cell  
312 tracks and speeds (Fig. 5, A to C, movie S7, A to E). As expected, FBS supplemented media  
313 significantly enhanced cell movement (Fig. 5, A to C and movie S7B). In contrast to collagen-  
314 I, fibronectin and collagen-IV, which showed strong effects on ILC2 dynamics, collagen-III,  
315 versican and tenascin C showed minimal influence on ILC2 movement (fig. S7A). Collagen  
316 fibres also produce contrast in two-photon microscopy by generating a strong second  
317 harmonic signal in tissue. Second harmonic generation (SHG) imaging suggested that the  
318 area around bronchioles and associated vessels had a strong fibrillar collagen component in  
319 both IL33-treated and control PCLS (Fig. 5D). We noticed a qualitative difference in the SHG  
320 signal with the collagen fibres in perivascular / peribroncheal areas of rIL-33 treated mice  
321 appearing 'spikier' than those in PBS treated control mice. Therefore, we analysed the  
322 geometry of the SHG images of fibrillar collagen in the perivascular / peribronchial area using  
323 a grey level co-occurrence matrix (GLCM) technique to quantify and compare the SHG signal  
324 (52, 53). Initially we plotted correlation versus comparison distance. This analysis compares  
325 the organisation of the extracellular matrix by considering how far it is possible to travel in a  
326 straight line away from a start point and observe the same intensity (grey level) between pairs  
327 of pixels. Images containing features that are generally organised in long straight lines will  
328 therefore have higher levels of intensity correlation over longer comparison distances and  
329 images that display structures more randomly orientated will lose this correlation at shorter  
330 comparison distances producing decays with steeper slopes. As can be seen from the data

331 (Fig. 5E) GLCM SHG analysis of the perivascular / peribronchial area from IL-33 treated mice  
332 gave steeper decays than the controls, indicating a more disordered arrangement of shorter  
333 fibres. We also plotted homogeneity versus comparison distance. This parameter considers  
334 the distribution of grey levels at different comparison distances across the image. Therefore,  
335 images that have a texture less consistent with long fibrillar structures will have steeper decays  
336 in homogeneity with comparison distance. These data (Fig. 5, D and E) also highlighted  
337 contrast between the two conditions.

338 In addition to collagen, fibronectin expression was also evaluated by staining for fibronectin in  
339 live PCLS from PBS or rIL-33 treated mice. Our results showed that fibronectin expression is  
340 enriched in the peribronchial region of rIL-33 treated mice (Fig. 5F). Collectively, our data  
341 indicate that collagen-I, -IV and fibronectin influence ILC2 speed *in vitro*. Furthermore,  
342 collagen and fibronectin are modified in areas where ILC2 accumulate during rIL-33 induced  
343 inflammation.

344

#### 345 **Collagen-I enhances ILC2 actin cytoskeletal remodelling and polarity**

346 ECM protein 'tracks' can define the path of motile cells through the tissue (54). We observed  
347 that ILC2 exhibited amoeboid-like movement after rIL-33 induced inflammation (Fig. 2 and 3  
348 F). Amoeboid cell movement involves induction of a simple polarized shape, dynamic  
349 pseudopod protrusion and retraction, flexible oscillatory shape changes, and rapid low-affinity  
350 crawling (55). Our results showed that ECM proteins collagen-I, fibronectin and collagen-IV  
351 promoted increased human ILC2 motility in a 2D migration assay. Therefore, we next tested  
352 whether each ECM protein directly influenced changes in ILC2 phenotype, cytokine production  
353 and shape change in the same 2D environment. We found that ILC2 GATA-3 expression (fig.  
354 S7B) and IL-5 production (Fig. S7C) remained comparable after incubation over collagen-I or  
355 collagen-IV. However collagen-I selectively induced the most pronounced ILC2 shape change  
356 with characteristically elongated ILC2 cell bodies visible (Fig. 6, A and B). In amoeboid  
357 movement, force generation (protrusion and contraction) and force transduction (adhesion),  
358 are controlled by actomyosin cytoskeletal remodelling (56). We imaged f-actin localisation and

359 quantified ILC2 shape after 12h on the different ECM. ILC2 seeded on collagen-I were highly  
360 polarised with areas of f-actin accumulation (Fig. 6B) and had significantly greater cell area  
361 and perimeter (Fig. 6, C and D). Taken together these data indicate that collagen-I influences  
362 ILC2 shape towards the pro-migratory exploratory phenotype we described *in vivo* (Fig. 2 and  
363 3 F).

364

365 **Blocking collagen fibrillogenesis *in vivo* increases ILC2 dynamics and reduces**  
366 **eosinophil accumulation in the inflamed lung.**

367 We have previously demonstrated that epithelial cell derived TGF- $\beta$ 1, induced after rIL-33  
368 treatment, can drive ILC2 movement (34). Furthermore, our results show that collagen-I  
369 significantly alters ILC2 shape by elongating the cell body (Fig. 6). TGF- $\beta$  has been shown to  
370 enhance collagen-I and III mRNA expression during remodeling and blocking collagen  
371 deposition restores baseline collagen levels (57). We observed changes to collagen geometry  
372 in the peribronchial space where ILC2 are highly dynamic after rIL-33 treatment (Fig. 5, D and  
373 E). Hence, we next investigated whether we could extend our findings from the 2D assays  
374 previously described in Fig 6 into *in vivo* 3D tissue by blocking newly synthesized collagen  
375 and measuring ILC2 movement after rIL-33 induced inflammation. The fibrillar structure of  
376 type 1 collagen morphology is stabilized by inter and intra molecular crosslinks initiated by  
377 lysyl oxidases whose expression can be inhibited by  $\beta$ -amino propionitrile (BAPN) (57).  
378 Following rIL-33 treatment, we administered BAPN i.p. Strikingly, mice that received rIL-33  
379 along with the collagen crosslinking inhibitor showed longer tracks depicted as individual  
380 tracks (Fig. 7A) and track overlay between treatments (Fig. 7B). Cell track quantification  
381 revealed that ILC2 from lungs of mice that were rIL-33 treated along with BAPN displayed  
382 increased ILC2 track speed (Fig. 7C), track length (Fig. 7D) and track displacement (Fig. 7E)  
383 compared to rIL-33 treated mice suggestive of a reduced interaction with the ECM.

384 Although addition of BAPN altered ILC2 motility in rIL-33 treated mice, ILC numbers only  
385 slightly reduced in the lungs (Fig. 7F) with comparable ILC2 numbers in the BAL (Fig. 7G) and  
386 blood (Fig. 7H). We additionally tested if BAPN directly activated ILC2 by evaluating cytokine



387 production by ex vivo sorted ILC2 from rIL-33 treated IL-13 eGFP mice. Our results showed  
388 that within the time frame of 36 h post incubation, IL-5 production by ILC2 remained  
389 unchanged after incubation with collagen-I + BAPN or collagen-I alone (fig. S8A). Interestingly  
390 addition, of rCCL8 to the cultures significantly increased IL-5 production (fig. S8A). We next  
391 evaluated if blocking collagen fibrillogenesis in rIL-33 treated mice impacted on the  
392 inflammatory infiltrate in the lungs and altered lung function. rIL-33 + BAPN treated mice had  
393 unchanged lung function (Fig. 8A) and comparable numbers of airway macrophages (Fig. 8B),  
394 dendritic cells (Fig. 8C), neutrophils (Fig. 8D) compared to mice treated with rIL-33 alone.  
395 Interestingly, blocking collagen fibrillogenesis in rIL-33 treated mice significantly reduced the  
396 frequency of eosinophils (Fig. 8E) and lung CCL24 levels (Fig. 8F) while eosinophil motility  
397 remained unaltered compared to mice treated with rIL33 treated alone (movie S8, A and B)  
398 and further quantified by track length (fig. S8B) and track speed (fig. S8C). We finally  
399 compared eosinophil accumulation in the peribronchial region of the lungs where ILC2  
400 accumulate and found significantly lower number of eosinophils as demonstrated by congo  
401 red staining (Fig. 8G and H).

402 Therefore, blocking newly synthesized collagen during rIL-33 treatment significantly changed  
403 ILC2 motility and the ensuing eosinophil accumulation. These data indicate that ILC2  
404 interactions with the ECM may impact their function and contribution to eosinophilic  
405 inflammation.

406

#### 407 **Discussion:**

408 Immune cell recruitment in inflammation involves emigration of activated leukocytes from the  
409 vasculature across inflamed endothelium into the tissue space through activation of specific  
410 effector programs (58). The ensuing response must be robust enough to control infection or  
411 repair damage but sufficiently restrained so as to prevent excessive tissue damage and  
412 pathology. Mucosal surfaces, such as the lung, constantly encounter potentially harmful  
413 threats in the form of microbes, allergens and pollutants that can damage lung tissue and  
414 impair normal physiological lung function. Group 2 innate lymphoid cells (ILC2) are central in

415 orchestrating type-2 immunity (28) and promoting tissue repair (13). We have previously  
416 shown that during lung inflammation, *in vivo* and *in vitro*, TGF- $\beta$  expression influences ILC2  
417 movement but the mechanisms which promote ILC2 migration are not well understood (34).  
418 Hence a more detailed spatio-temporal analysis of ILC2 induction and dynamics in the lung is  
419 of great importance to develop a thorough appreciation of ILC2 behaviour and function, and  
420 their interaction with other cells during type 2 inflammatory responses. Since ILC2 are a rare  
421 immune cell population in the lung at homeostasis (28), visualizing ILC2 by intravital imaging  
422 in the lungs of living animals has been challenging. Delivery of rIL-33 in mice drives type-2  
423 immunity and ILC2 expand robustly and produce large amounts of IL-13 (28, 34) even in the  
424 absence of T and B cells (42). In this report, by utilizing a model of rIL-33 or Alt driven lung  
425 inflammation in IL-13eGFP knock-in mice, combined with sophisticated lung imaging, we  
426 demonstrate for the first time that ILC2 are highly dynamic in the lung *in vivo*. Following an  
427 acute inflammatory exposure, ILC2 numbers in the lung increased substantially by around 30  
428 (Alt) - 100 (rIL-33) fold respectively. Simultaneously, our results show an incremental increase  
429 in the number of ILC2 in both the lung draining LN and circulation after Alt or rIL-33 induced  
430 inflammation. A recent study reported that administration of rIL-33 in mice promotes the egress  
431 of ILC2 progenitors (ILC2Ps) from the bone marrow to peripheral tissues while mice lacking  
432 IL-33 signalling had a significant accumulation of ILC2Ps in the bone marrow (59). This  
433 suggests that the rapid expansion in ILC2 numbers induced in the lung in our model of rIL-33  
434 inflammation could result as a consequence of recruitment of ILC2Ps from the BM rather than  
435 *in situ* proliferation of a small steady state resident precursor. In addition, there was no  
436 increase in ILC2 numbers in the spleen or non-lung draining lymph nodes indicating that  
437 intranasal rIL-33 signals for ILC precursors in the bone marrow to traffic to the lungs. Our  
438 imaging studies also depict ILC2 accumulation in the extra-vascular tissue surrounding large  
439 blood vessels again indicating that these cells are perhaps likely to be recent emigrants from  
440 the BM.

441

442 In the lung, we found that ILC2 mainly accumulate in the peribronchial / perivascular area and  
443 to a lesser extent in the parenchyma. The location of ILC2 in the peribronchial area is  
444 consistent with their postulated role in promoting epithelial repair. In a previous study, we  
445 showed that ILC2 in the airway lumen are primed to respond to epithelial cell derived TGF- $\beta$   
446 induced after rIL-33 administration, as a result of high cell surface expression of TGF- $\beta$ RII,  
447 and that epithelial cell derived TGF- $\beta$  enhanced the migratory activity of ILC2 (34). Hence a  
448 critical molecular communication exists between ILC2 and bronchial epithelial cells to promote  
449 ILC2 movement during lung inflammation and could explain why ILC2 home to the  
450 peribronchial region of the lung tissue.

451

452 By using live lung slices, we demonstrated an amoeboid pattern of movement of lung ILC2  
453 after rIL-33 treatment. This observation was recapitulated in the lungs of live intact mice using  
454 lung intravital microscopy of rIL-33 treated IL13eGFP mice. We found that similar to our data  
455 in live lung slices, ILC2 were enriched in the lung tissue surrounding larger blood vessels  
456 rather than the alveolar capillaries and characteristically move in an amoeboid manner during  
457 locomotion. However, despite their functional and phenotypic similarities to CD4<sup>+</sup> T cells,  
458 ILC2 differed markedly in their migratory behaviour moving faster and to greater distances  
459 than CD4<sup>+</sup> T cells in the inflamed lung. The physical proximity of motile ILC2 to epithelial  
460 cells further supports the notion that ILC2 may directly influence epithelial cell function and  
461 vice versa and may not be restricted to communication via secreted cytokines but could  
462 result from physical receptor-ligand interactions. It is known that motility patterns and  
463 distances travelled by various leukocyte subpopulations differ (60). In our study, we find that  
464 lung ILC2 exhibit amoeboid pattern of movement travelling distances in the range of 100-  
465 200 $\mu$ m perhaps displaying 'searching' or 'exploratory' behaviour, consistent with their  
466 sentinel role at mucosal sites (61). Taken together, our data suggests that lung ILC2 may  
467 exhibit motility patterns similar to innate immune cells. This is consistent with findings in the  
468 skin, where dermal ILC2 patrol their environment with an average speed similar to that of  
469 dermal dendritic cells (38). This scanning behaviour of ILC2 may be suggestive of their need

470 to detect local alarmins or danger signals by damaged epithelial cells in the lung after an  
471 inflammatory insult. Furthermore, the migration of lung ILC2 in close association with bronchial  
472 epithelial cells seems likely to ensure that factors secreted by the epithelium, such as TGF- $\beta$ ,  
473 can rapidly engage the ILC2. It presumably also ensures that signalling in the reverse  
474 direction, from the ILC2 to the epithelial cells, for promoting epithelial repair can take place  
475 efficiently.

476

477 Factors driving leukocyte motility include the distribution of adhesion molecules on leukocytes,  
478 as well as chemotactic signals. It has been well established that lung ILC2 express both  $\beta$ 1  
479 and  $\beta$ 2 integrins at homeostasis and after Alt-induced inflammation (39). Furthermore, ILCs  
480 share many of the key features analogous to T cell populations, for example ILC2 and T cells  
481 both use the homing receptor CCR7 to actively migrate to lymphoid tissues (3). In addition, it  
482 has been shown recently that inflammatory iILC2, originating from precursors in the intestinal  
483 lamina propria express high levels of CCR9 and use sphingosine 1-phosphate receptors to  
484 exit the intestine into the lymph and move to distant sites like the lung where they display  
485 effector activity (15). Interestingly, progenitors to iILC2 do not exist in the lung and are not  
486 induced after inflammation induced via the intra nasal route (15). Hence, the chemokine  
487 migratory programs of ILC2 generated in the lung after intranasal instilled mediator driven  
488 inflammation have remained elusive until now and very little is understood about the process  
489 by which ILC2 are attracted to sites of immune insult in the lungs. At homeostasis, we found  
490 that CCR8 and CCR1 was expressed by the majority of murine lung ILC2, in contrast to other  
491 T cell subsets. However, following rIL-33 treatment, the percentage of CCR8 and CCR1  
492 expressing ILC2 further increased.

493

494 In addition, TGF- $\beta$  acts as an ILC2 chemo-activator enhancing murine ILC2 migration in a  
495 non-directional manner. Furthermore, both PGD<sub>2</sub> and to a much lesser extent IL-33 have been  
496 shown to be chemotactic for human skin- and blood-derived ILC2 (48). Interestingly, we show

497 for the first time that in addition to PGD2, CCL8 is chemotactic for ILC2 with nanomolar  
498 potency. We found that CCL8 deposits were strongly expressed in the peribronchial space  
499 where murine lung ILC2 accumulate. This could be attributed to the CCL8–CCR8 ligand-  
500 receptor axis which has been shown to be crucial in localizing pathogenic Th2 cells to the site  
501 of eosinophilic inflammation and in driving the allergic process in the skin (62). To further  
502 explore this hypothesis, we blocked CCR8 receptor in rIL-33 treated mice and analysed effects  
503 on ILC2 motility. Our data strongly suggest that signalling via CCR8 is critical for ILC2 cytokine  
504 (IL-13 and IL-5) production as well as motility of IL-13<sup>+</sup> activated ILC2. A variety of resident  
505 pulmonary cells secrete CCL8, the CCR8 ligand in mice. We find that lung airway  
506 macrophages are the pre-dominant cellular source of CCL8 in rIL-33 treated mice. Our data  
507 suggest a previously undescribed model where macrophage derived CCL8 acts **to increase**  
508 **ILC2 accumulation** to areas proximal to epithelial cells.

509

510 Overall, our results provide insights into the independent and distinct migration pathways ILC2  
511 utilize in contrast to T cells. Extracellular matrix proteins such as collagens are well-known to  
512 interact with leukocytes by directly binding to cell surface receptors (63). In this respect,  
513 changes to subepithelial collagen and extracellular matrix protein deposition are important  
514 pathophysiological components of airway remodeling in Th2 driven lung inflammation. We find  
515 strong fibrillar collagen deposition around bronchioles and associated vessels in both rIL33-  
516 treated and control PCLS where lung ILC2 accumulate. Interestingly rIL-33 treated mice  
517 showed quantitative differences in both correlation and homogeneity parameters of fibrillar  
518 collagen geometry compared to control mice. rIL-33 induced epithelial TGF- $\beta$  is chemoactive  
519 for ILC2 and administration of TGF- $\beta$  in mice increases collagen-I mRNA expression in mouse  
520 lungs (49, 57). This suggests that altered collagen distribution as a result of rIL-33 induced  
521 inflammation may influence ILC2 migratory programs. In line with this, our *in vitro* 2D migration  
522 assays indicate that collagen-I exclusively alters ILC2 morphology with enhanced cell spread  
523 and elongation of cell body. Hence *in vivo*, collagen-I fibres may support a more polarized

524 ILC2 morphology, by increasing ILC2 traction, reducing ILC2 speed and allowing for longer  
525 dwell times in specific sites of inflammation in the lung. Cross-links are essential for the  
526 mechanical stability of collagen and have been shown to control T cell mobility (64). To test  
527 the overall contribution of newly synthesized collagen on ILC2 dynamics, we used beta-  
528 aminopropionitrile (BAPN) to block the formation of new collagen cross-links by inhibiting the  
529 enzyme lysyloxidase. Interestingly, blockade of collagen fibrillogenesis significantly increased  
530 ILC2 speed and travel distance after rIL-33 treatment. Hence suggesting that reduced collagen  
531 stability, resulting as a consequence of blocking new collagen fibrillogenesis may disrupt a  
532 controlled receptor-ligand interaction of ILC2 with collagen-I fibres, increasing overall  
533 dynamics of ILC2. Intriguingly, although collagen-I blocking increased ILC2 movement, rIL-33  
534 induced eosinophilia was significantly reduced in the lungs of these mice. We have previously  
535 reported that after house dust mite treatment in mice, chemoactive epithelial derived TGF- $\beta$  is  
536 essential for ILC2 activation and critically controls all hallmarks features of allergic responses  
537 including airway hyperresponsiveness and eosinophilia (34). Inferring from this knowledge our  
538 data suggests that although the initial cytokine driven instruction from structural cells initiates  
539 ILC2 movement, components of the inflamed lung environment namely, CCL8-CCR8  
540 signaling and collagen-I are critical for regulating controlled **ILC2 accumulation** and dynamics  
541 imperative for ensuring robust type-2 inflammation. Hence although TGF- $\beta$  serves as a  
542 chemokinetic mediator, CCL8 induced after rIL-33 treatment is an important chemotactic  
543 signal that mediates ILC2 motility and cytokine production via CCR8 receptor. Furthermore,  
544 the difference in interfibrillar geometry of collagen fibrils alters ILC2 migratory patterns and the  
545 dwell time of ILC2 with collagen-fibrils is a critical factor towards ILC2 behaviour and function  
546 in type-2 inflammation. Thus combined environmental signals from damaged lung tissue act  
547 in concert to mechanistically drive ILC2 migratory patterns in the inflamed lung.

548

549 ILC2 are defined by the combination of several extracellular and intracellular markers. Here  
550 we use multicolour flow cytometry of cell suspensions from dissociated lung tissue to identify  
551 and quantify these cells, but this approach loses spatiotemporal information by

552 definition. Therefore, we used a combination of imaging using IL13-GFP reporter mice in  
553 combination with a handful of markers and dyes and detailed multicolour flow cytometry  
554 together to mitigate potential misidentification of the cells. However, in an ideal experiment  
555 we would be able to image tens of markers simultaneously. Newer approaches (for eg:  
556 imaging mass cytometry) are starting to address this, but none allow live organism / cell /  
557 tissue imaging to directly address the spatiotemporal dynamics of these populations, a  
558 significant challenge in the field.

559  
560 Overall, using highly sophisticated imaging techniques, we reveal how ILC2 migrate within  
561 an inflamed tissue, interact with adjacent cells and lung environmental factors during a type-  
562 2 inflammatory response. Specifically, we show that lung ILC2 are highly motile *in vivo* and  
563 exhibit an exploratory amoeboid pattern of movement during inflammation. Additionally, we  
564 identify signature chemokine receptors employed by ILC2 to home to inflammatory sites in the  
565 lung. Our data provide novel insights into the mechanism by which diverse lung environmental  
566 factors combine to control ILC2 migration and provide direct evidence for collagen-I  
567 exclusively regulating ILC2 shape and polarity, thereby influencing the outcome of an  
568 inflammatory response. Imaging these dynamic cellular events in real-time in the lungs of  
569 living animals has provided an important visual platform that could be employed for further  
570 interrogation of ILC2 and other immune cell functions in the context of allergen or pathogen  
571 driven Th2 inflammation.

572

573

## 574 **Materials and Methods**

575

### 576 **Mice**

577 Adult female IL13-eGFP (kind gift from A.N. McKenzie, MRC Laboratory of Molecular Biology,  
578 Cambridge) (28) were used for experiments between 7 and 10 weeks of age. Mice were  
579 housed in specific-pathogen-free conditions and given food and water ad libitum. All  
580 procedures were conducted in accordance to the institutional guidelines and under the

581 approval of our Home Office project licence (granted under the Animals (Scientific Procedures)  
582 Act 1986). Mice were administered 10µg (*Alternaria alternata*) extract (Greer Laboratories) in  
583 25µl of PBS intranasally 3 times a week for 1 week or PBS alone as controls. Alternatively,  
584 carrier-free recombinant murine rIL-33 (1µg per dose in 25µl PBS) (eBioscience) or PBS was  
585 administered 3 times a week for 1 week. Mice were culled 24hrs after the final cytokine or  
586 allergen dose.

587

### 588 **Live Precision Cut Lung Slices**

589 Ex vivo cultured precision-cut lung slices (PCLS) provided a 3D cell culture model to image  
590 ILC2 dynamics within the lung microenvironment and was adapted and modified from a  
591 previously described protocol (65). Briefly, prior to slicing, lungs were inflated with 0.8ml  
592 volume of 2% low melting agarose (ThermoFisher) prepared in PBS. Following inflation lungs  
593 were carefully dissected out and placed in HBSS containing 2.5% HEPES (GIBCO, Life  
594 Technologies). The intact left superior lung lobe was excised and 200µm transverse sections  
595 were prepared from the upper 1mm region of the left superior lung lobe using a Compressome  
596 VF-300 vibrating microtome (Precisionary Instruments). PCLS were incubated in complete  
597 RPMI (10% FCS, 2 mM L-glutamine, 100U/ml penicillin/streptomycin) (GIBCO, Life  
598 Technologies) for 15mins at 37°C to wash off excess agarose surrounding the tissue.  
599 Antibodies were prepared in complete DMEM solution and lung explants were incubated in  
600 staining solution for 1.5hrs at 37°C prior to imaging. Time lapse videos depicting ILC2  
601 movement were generated over an hour using an inverted laser-scanning confocal  
602 microscope (SP5, Leica microsystems). Videos were quantified using Imaris version 8.1  
603 (BitPlane, Oxford Instruments) and ILC2 track speed, length and displacement were quantified  
604 using Motilitylab software.

605

606 **Table S1. Antibodies used for imaging of PCLS**

Antibody	Clone	Fluorochrome	Target species	Manufacturer
EPCAM	G8.8	PE	Mouse	Biologend



CD4	RM4-5	BV421	Mouse	Biolegend
CD31	390	Alexa-647	Mouse	Biolegend

607

### 608 **Intravital microscopy**

609 Mouse lung intravital microscopy was performed as previously described (44, 66). Briefly,  
610 anaesthetised and mechanically ventilated mice were placed on a heat-mat in a right lateral  
611 position. A small custom-built circular suction chamber was surgically inserted using a small  
612 incision between the ribs of the mice for imaging on an upright laser-scanning confocal  
613 microscope with Hybrid detectors (Leica SP5). Gentle suction was applied via the vacuum  
614 port to bring the cover slip contained in the chamber into contact with the lung and stabilise  
615 the tissue. Time-lapse videos depicting ILC2 movement were generated using 488, 54 and  
616 633nm laser lines through a 25x 0.95 N.A. long working distance water immersion objective.

617

### 618 **Fixed Cell / PCLS imaging**

619 Phalloidin stained ILC and fixed PCLS from IL-33 reported mice were imaged using a Zeiss  
620 LSM 880 Airyscan NLO system. DAPI was excited using a 405nm diode laser, Phalloidin  
621 AlexaFlour488 was excited at 488nm using an argon-ion laser and detected using a sub-Airy  
622 detector 32-element array (Airyscan) and processed using 'auto' 3D Airyscan processing  
623 options. Airyscan z-stacks were acquired and Imaris (Bitplane) was used to visualise each  
624 cell. SHG signals (produced at a central wavelength of 475nm) were collected from fixed PCLS  
625 using a Coherent Chameleon Discovery femtosecond pulsed laser tuned to 950 nm and  
626 collected using a non-descanned GaAsP detector with 450±50nm detection filter. A 25x 1.0  
627 N.A. zeiss long working distance water immersion objective was used to collect all images.

628

629

### 630 **SHG Analysis**

631 50µm z-stacks were imaged over a region of 425.1µm by 425.1, with at least three stacks  
632 /mouse (n = 6 mice / condition). GLCM was performed similarly to previous studies (67, 68)

633 Briefly, Image J (NIH) and the Norwegian University of Life Sciences (UMB) GLCM plugin was  
634 used for the texture analysis, modified to run automatically through the four directions, for each  
635 of the 100 comparison distances. A maximum projection image was automatically thresholded  
636 to produce a mask that was then applied to remove background noise bias in the GLCM  
637 analysis by selecting only the collagen SHG signal. The masked image was then passed to  
638 the modified GLCM texture plugin. The data files produced were processed using an ImageJ  
639 macro to output both the mean and individual values for each texture parameter for each  
640 image. These were then imported into Prism (GraphPad), where exponential decay models  
641 were fitted to the data.

642

#### 643 **Cell isolation (BAL, Lung and lung dLN)**

644 The airways were washed three times with 400µl of PBS and bronchoalveolar lavage fluid was  
645 collected. Following centrifugation of the BAL fluid supernatants were stored at -80°C for  
646 further analysis and cells were resuspended in 500µl of complete RPMI media (10% FCS,  
647 2mM L-glutamine, 100U/ml penicillin/streptomycin) (GIBCO, Life Technologies). For lung cell  
648 isolation, the left lung lobes were cut into small pieces and digested in complete media  
649 supplemented with 0.15mg/ml collagenase (Type D; Roche Diagnostics) and 25µg/ml DNase  
650 (Type 1; Roche Diagnostics) for 1h at 37°C. Lung homogenate obtained was then filtered  
651 through a 70µm sieve (BD Bioscience), washed, and resuspended in 1ml of complete media.  
652 Erylysis was performed on 200µl whole blood and leukocytes were washed twice and then  
653 then resuspended in 1ml of complete media.

654

#### 655 **Flow Cytometry and intracellular staining**

656 For phenotyping ILC2 in IL-13 eGFP mice by flow cytometry, ILC2 were defined as live, singlet,  
657 lymphoid, GFP<sup>+</sup>CD45<sup>+</sup> lineage<sup>neg</sup> (Lineage cocktail: TCRβ, TCRγδ, CD3e, CD5, CD19,  
658 CD11b, CD11c, FCεR1, GR-1, F4/80, NKp46 and TER-119) CD3<sup>-</sup> NKp46<sup>-</sup>,  
659 CD90.2<sup>+</sup>/CD127<sup>+</sup>/KLRG1<sup>+</sup>/CD25<sup>var</sup> cells with positive intracellular IL-13 and IL-5 staining.

660

661 For intracellular cytokine staining, cells were stimulated with PMA (Sigma-Aldrich) and  
662 ionomycin (EMD Chemicals) in the presence of Brefeldin A (Sigma-Aldrich) and incubated for  
663 4h at 37°C. Following stimulation, cells were washed and incubated for 20min with anti-  
664 CD16/32 (BD Pharmingen) prior to staining for extracellular antigens in 5% FCS/1% BSA in  
665 PBS for 30min at 4°C. All antibodies were purchased from eBioscience (table 2) with the  
666 exception of CD31, EpCAM, CD4 (Biolegend) also shown in table 1. Following staining for  
667 extracellular markers, cells were fixed with IC fixation buffer (E-Bioscience) for 10 mins at  
668 room temperature. Cells were then washed and stained for intracellular antigens using the  
669 Intracellular Fixation & Permeabilization Buffer Set (E Bioscience) or Foxp3 / Transcription  
670 Factor Staining Buffer Set (E-Bioscience) for GATA-3 staining.  
671 Analysis was performed with LSRFortessa III and cell sorting on FACSAria III (BD  
672 Biosciences).

673

674 **Table S2. Antibodies used for flow cytometry**

675

Antibody	Clone	Fluorochrome	Target species	Manufacturer	
TCR-β	H57-597	APC	Mouse	E Bioscience	
TCR-γδ	ebio GL3	APC	Mouse	E Bioscience	
TER-119	TER-119	APC	Mouse	E Bioscience	
CD19	ebio ID3	APC	Mouse	E Bioscience	
CD11b	M1/70	APC	Mouse	E Bioscience	
CD5	53-7.3	APC	Mouse	E Bioscience	
F4/80	BM8	APC	Mouse	E Bioscience	
FCεR1	MAR1	APC	Mouse	E Bioscience	
GR-1	RB6-8C5	APC	Mouse	E Bioscience	
CD11c	N418	APC	Mouse	E Bioscience	
NKp46	29A1.4	PE-Dazzle	Mouse	E Bioscience	

CD45	30-F11	PerCP Cy5.5	Mouse	E Bioscience	
CD3e	145-2C11	APC-Cy7	Mouse	E Bioscience	
KLRG-1	2F1/KLRG1	PE-Cy7	Mouse	E Bioscience	
CD90.2	53-2.1	BV605	Mouse	E Bioscience	
CD25	PC61	BV510	Mouse	E Bioscience	
CD127	A7R34	BV711	Mouse	E Bioscience	
IL-13	ebio 13A	PE	Mouse	E Bioscience	
IL-5	TRFK5	BV421	Mouse	E Bioscience	
GATA-3	TWAJ	PerCP-eFluor 710	Mouse	E Bioscience	

676

677

678 **Lung histology and staining**

679

680 Paraffin embedded lung sections (4-micron thickness) were stained with haematoxylin and  
681 Congo red-dyes. Images were taken under polarised light using an upright dry 40x objective.  
682 The number of eosinophils in the peribronchial space were quantified and corrected for the  
683 surface area scored.

684

685 **Human ILC2 bulk cultures**

686 ILC2 were enriched from whole blood using RosetteSep™ Human ILC2 Enrichment Kit  
687 (STEMCELL Technologies) and further sorted by FACs using CD45<sup>+</sup> Lineage<sup>neg</sup> (CD1a, CD3,  
688 CD4, CD5, CD8, CD11c, CD14, CD16, CD19, CD20, CD34, FcγRI and CD123) (Biolegend),  
689 CD161<sup>+</sup>, CD127<sup>+</sup>, CRTH2<sup>+</sup> and C-Kit<sup>var</sup> (Biolegend). ILC2 were bulk cultured in IL-2, IL-7  
690 (5ng/ml) and IL-33 (10ng/ml) (eBioscience) and cytokines and medium were replenished  
691 every 3-4 days. For investigations involving humans ILC2 isolation, an informed consent was  
692 obtained and the nature and possible consequences of the studies were explained to all  
693 donors.

694

695 **Table S3. Antibodies used for sorting human ILC2**

696

Antibody	Clone	Fluorochrome	Target species	Manufacturer
CD11c	3.9	FITC	Human	Biologend
CD123	6H6	FITC	Human	Biologend
CD14	63D3	FITC	Human	Biologend
CD16	B73.1	FITC	Human	Biologend
CD161	HP-3G10	PECy7	Human	Biologend
CD19	HIB19	FITC	Human	Biologend
CD1a	HI149	FITC	Human	Biologend
CD20	2H7	FITC	Human	Biologend
CD3	OKT3	FITC	Human	Biologend
CD34	581	FITC	Human	Biologend
CD4	OKT4	FITC	Human	Biologend
CD5	L17F12	FITC	Human	Biologend
CD127	A019D5	PerCP5.5	Human	Biologend
CRTH2	BM16	BV421	Human	Biologend
CD45	H130	BV605	Human	Biologend

697

698 **CCR8 antibody blocking and rCCL8 treatment**

699 CCR8 neutralisation studies were performed similar to previous reports (69). IL-13eGFP and  
700 balb/c mice were i.p. injected with 5 $\mu$ g purified anti-mouse CD198 (CCR8) antibody, (Clone:  
701 SA214G2) or purified Rat IgG2b,  $\kappa$  Isotype Ctrl Antibody two days prior to first dose of rIL-33  
702 treatment and then combined with each of the three rIL-33 doses. Mice were analysed 24h  
703 post the third dose. Alternately 10 $\mu$ g Recombinant Mouse CCL8 (MCP-2) (Biologend) was  
704 administered i.n. at the time of the three rIL-33 doses.

705

706  **$\beta$ -aminopropionitrile (BAPN) treatment**

707 BAPN treatment was carried out similar to previous reports (70). IL-13 eGFP or balb/c mice  
708 were i.p. injected with  $\beta$ -aminopropionitrile (BAPN) (100 mg/kg, Sigma) dissolved in PBS and  
709 administered in 200  $\mu$ l volume on day -1 and then daily for a week over the course of rIL-33  
710 treatment.

711

712 **Measurement of Airway hyperresponsiveness**

713 Airway resistance in mice was evaluated adopting the flexiVent small animal ventilator  
714 (SciReq) as previously described (29) Prior to procedure mice were anesthetized with a  
715 combination of pentobarbital sodium (50 mg/kg, administered intraperitoneally) and ketamine  
716 (100 mg/kg, administered intramuscularly), tracheostomized, and connected to the flexiVent  
717 ventilator using a blunt-ended 19-gauge needle. The mice were ventilated by maintaining an  
718 average breathing frequency of 150 breaths/min, tidal volume of 10 ml/kg body weight and  
719 positive end-expiratory pressure of about 2 cm H<sub>2</sub>O. Differences in resistance to increasing  
720 concentrations of nebulized methacholine (3- 100 mg/ml) were analysed from the snap-shot  
721 perturbation measurements. The data was then plotted using multiple linear regression to the  
722 single-compartment model in the following form: pressure = resistance  $\times$  flow + elastance  $\times$   
723 volume + fitting constant.

724

725 **Chemotaxis Assay**

726 Assays of chemotactic responsiveness were carried out as previously described using 96-well  
727 ChemoTx® plates with 5 $\mu$ m pores (Neuroprobe). Migrating cells were detected by the use of  
728 CellTiterGlo® Dye (Promega) and resulting luminescence measured using a TopCount  
729 scintillation counter (PerkinElmer). In all experiments, each data point was assayed in  
730 duplicate. Data are reported as Chemotactic Indices, defined as the migratory response to a  
731 particular stimulus divided by the migratory response to media alone.

732

733 **Analysis of ILC2 dynamics on ECM proteins**

734 Human ILC2 were obtained by sorting and differentiating ILC2 from peripheral blood. ILC2  
735 lines were seeded on tissue culture plates coated with 10% FBS, 50µg/ml of fibronectin,  
736 collagen-I, and -IV. Human ILC2 dynamics was imaged on the JuLI imaging system for a  
737 period of 12h. ILC2 dynamics quantified as changes in speed and displacement were  
738 quantified using Image J software.

739

740 **Statistical analysis**

741 All data were analyzed using Graph Pad Prism 7. Time series videos were analysed and cell  
742 tracks were quantified by Imaris software. Tracks were imported to Prism for quantifying track  
743 length and track speed. Additionally tracks were imported into MotilityLab software to display  
744 tracks from centroid and differences in mean square displacement. All line graphs and bar  
745 charts are expressed as mean ±SD and data analyzed with non-parametric Mann-Whitney U  
746 test where significance was defined as \*p < 0.05, \*\*p < 0.01, \*\*\*p < 0.001 and,\*\*\*\* p < 0.0001.

747

748 **Supplementary Materials**

749

750 Figure S1 Gating strategy for identification of ILC2 populations, related to Fig. 1 A-C.

751 Figure S2. Quantification of ILC2 in different tissues, related to Fig. 1 A-C.

752 Figure S3. Gating strategy for identification of ILC2 populations based on GATA-3 expression,  
753 related to Fig. 1 A-C.

754 Figure S4. Distribution of ILC2 and CD4<sup>+</sup> T cells in rIL33 treated mice lungs, related to Fig. 1  
755 D and F.

756 Figure S5. Chemokine receptor expression on ILC, related to Fig 4. (A-B).

757 Figure S6. Phenotype and IL-13 production by human ILC2 lines, related to figures 4 and 5.

758 Figure S7. ILC2 motility on extracellular matrix proteins, collagen-III and proteoglycans  
759 Versican and tenascin-C, related to figure 5A-C.

760 Figure S8. BAPN fails to affect ILC2 cytokine production and eosinophil movement, related to  
761 figure 8G.

762 Movie S1. Time-lapse imaging of rIL-33 treated mouse lung PCLS showing ILC2 movement  
763 and location, related to Fig. 2 A.

764 Movie S2. Time-lapse imaging of rIL-33 treated mouse lung PCLS depicting differences in  
765 movement of independent ILC2, related to Fig. 2 B.

766 Movie S3. Time-lapse imaging of rIL-33 treated mouse lung PCLS depicting high power videos  
767 differences in movement of independent ILC2, related to Fig. 2 C.

768 Movie S4. Intra-vital imaging of rIL-33 treated mouse lung depicting amoeboid ILC2  
769 movement, related to Fig. 2 H.

770 Movie S5. Influence of ILC2 survival and cytokines on ILC2 motility, related to figure 5A-C.

771 Movie S6. Time-lapse imaging of lung PCLS from rIL-33 treated mouse treated with anti-CCR8  
772 Ab or Isotype Ab, related to Fig. 4I.

773 Movie S7. Collagen-I induced ILC2 shape change and elongation of cell body, related to Fig.  
774 5 A.

775 Movie S8. Time-lapse imaging of a lung PCLS assessing the effect of BAPN on rIL-33 treated  
776 mouse lung eosinophil movement, related to Fig. 8G.

777

## 778 **References**

779

780 1. M. G. Constantinides, B. D. McDonald, P. A. Verhoef, A. Bendelac, A committed precursor to  
781 innate lymphoid cells. *Nature* **508**, 397-401 (2014).

782 2. N. Serafini, R. G. Klein Wolterink, N. Satoh-Takayama, W. Xu, C. A. Vosshenrich, R. W. Hendriks,  
783 J. P. Di Santo, Gata3 drives development of ROR $\gamma$ mat+ group 3 innate lymphoid cells. *J Exp*  
784 *Med* **211**, 199-208 (2014).

785 3. C. H. Kim, S. Hashimoto-Hill, M. Kim, Migration and Tissue Tropism of Innate Lymphoid Cells.  
786 *Trends Immunol* **37**, 68-79 (2016).

787 4. J. K. Bando, H. E. Liang, R. M. Locksley, Identification and distribution of developing innate  
788 lymphoid cells in the fetal mouse intestine. *Nat Immunol* **16**, 153-160 (2015).

789 5. H. Spits, T. Cupedo, Innate lymphoid cells: emerging insights in development, lineage  
790 relationships, and function. *Annu Rev Immunol* **30**, 647-675 (2012).

791 6. C. S. Klose, D. Artis, Innate lymphoid cells as regulators of immunity, inflammation and tissue  
792 homeostasis. *Nat Immunol* **17**, 765-774 (2016).

793 7. A. N. J. McKenzie, H. Spits, G. Eberl, Innate lymphoid cells in inflammation and immunity.  
794 *Immunity* **41**, 366-374 (2014).



- 795 8. N. Serafini, C. A. Vosshenrich, J. P. Di Santo, Transcriptional regulation of innate lymphoid cell  
796 fate. *Nat Rev Immunol* **15**, 415-428 (2015).
- 797 9. G. F. Sonnenberg, D. Artis, Innate lymphoid cells in the initiation, regulation and resolution of  
798 inflammation. *Nat Med* **21**, 698-708 (2015).
- 799 10. R. Jones, E. J. Cosway, C. Willis, A. J. White, W. E. Jenkinson, H. J. Fehling, G. Anderson, D. R.  
800 Withers, Dynamic changes in intrathymic ILC populations during murine neonatal  
801 development. *Eur J Immunol* **48**, 1481-1491 (2018).
- 802 11. D. Artis, H. Spits, The biology of innate lymphoid cells. *Nature* **517**, 293-301 (2015).
- 803 12. G. Eberl, M. Colonna, J. P. Di Santo, A. N. McKenzie, Innate lymphoid cells. Innate lymphoid  
804 cells: a new paradigm in immunology. *Science* **348**, aaa6566 (2015).
- 805 13. L. A. Monticelli, G. F. Sonnenberg, M. C. Abt, T. Alenghat, C. G. Ziegler, T. A. Doering, J. M.  
806 Angelosanto, B. J. Laidlaw, C. Y. Yang, T. Sathaliyawala, M. Kubota, D. Turner, J. M. Diamond,  
807 A. W. Goldrath, D. L. Farber, R. G. Collman, E. J. Wherry, D. Artis, Innate lymphoid cells  
808 promote lung-tissue homeostasis after infection with influenza virus. *Nat Immunol* **12**, 1045-  
809 1054 (2011).
- 810 14. J. C. Nussbaum, S. J. Van Dyken, J. von Moltke, L. E. Cheng, A. Mohapatra, A. B. Molofsky, E. E.  
811 Thornton, M. F. Krummel, A. Chawla, H. E. Liang, R. M. Locksley, Type 2 innate lymphoid cells  
812 control eosinophil homeostasis. *Nature* **502**, 245-248 (2013).
- 813 15. Y. Huang, K. Mao, X. Chen, M. A. Sun, T. Kawabe, W. Li, N. Usher, J. Zhu, J. F. Urban, Jr., W. E.  
814 Paul, R. N. Germain, S1P-dependent interorgan trafficking of group 2 innate lymphoid cells  
815 supports host defense. *Science* **359**, 114-119 (2018).
- 816 16. G. Gasteiger, X. Fan, S. Dikiy, S. Y. Lee, A. Y. Rudensky, Tissue residency of innate lymphoid  
817 cells in lymphoid and nonlymphoid organs. *Science* **350**, 981-985 (2015).
- 818 17. H. K. Kim, S. Lund, R. Baum, P. Rosenthal, N. Khorram, T. A. Doherty, Innate type 2 response  
819 to *Alternaria* extract enhances ryegrass-induced lung inflammation. *Int Arch Allergy Immunol*  
820 **163**, 92-105 (2014).
- 821 18. K. Moro, H. Kabata, M. Tanabe, S. Koga, N. Takeno, M. Mochizuki, K. Fukunaga, K. Asano, T.  
822 Betsuyaku, S. Koyasu, Interferon and IL-27 antagonize the function of group 2 innate lymphoid  
823 cells and type 2 innate immune responses. *Nat Immunol* **17**, 76-86 (2016).
- 824 19. A. H. Lei, Q. Xiao, G. Y. Liu, K. Shi, Q. Yang, X. Li, Y. F. Liu, H. K. Wang, W. P. Cai, Y. J. Guan, D. I.  
825 Gaborilovich, J. Zhou, ICAM-1 controls development and function of ILC2. *J Exp Med* **215**, 2157-  
826 2174 (2018).
- 827 20. T. A. Doherty, D. Scott, H. H. Walford, N. Khorram, S. Lund, R. Baum, J. Chang, P. Rosenthal, A.  
828 Beppu, M. Miller, D. H. Broide, Allergen challenge in allergic rhinitis rapidly induces increased  
829 peripheral blood type 2 innate lymphoid cells that express CD84. *J Allergy Clin Immunol* **133**,  
830 1203-1205 (2014).
- 831 21. J. L. Barlow, A. Bellosi, C. S. Hardman, L. F. Drynan, S. H. Wong, J. P. Cruickshank, A. N.  
832 McKenzie, Innate IL-13-producing nuocytes arise during allergic lung inflammation and  
833 contribute to airways hyperreactivity. *J Allergy Clin Immunol* **129**, 191-198 e191-194 (2012).
- 834 22. K. R. Bartemes, K. Iijima, T. Kobayashi, G. M. Kephart, A. N. McKenzie, H. Kita, IL-33-responsive  
835 lineage- CD25+ CD44(hi) lymphoid cells mediate innate type 2 immunity and allergic  
836 inflammation in the lungs. *J Immunol* **188**, 1503-1513 (2012).
- 837 23. K. R. Bartemes, G. M. Kephart, S. J. Fox, H. Kita, Enhanced innate type 2 immune response in  
838 peripheral blood from patients with asthma. *J Allergy Clin Immunol* **134**, 671-678 e674 (2014).
- 839 24. S. G. Smith, R. Chen, M. Kjarsgaard, C. Huang, J. P. Oliveria, P. M. O'Byrne, G. M. Gauvreau, L.  
840 P. Boulet, C. Lemiere, J. Martin, P. Nair, R. Sehmi, Increased numbers of activated group 2  
841 innate lymphoid cells in the airways of patients with severe asthma and persistent airway  
842 eosinophilia. *J Allergy Clin Immunol* **137**, 75-86 e78 (2016).
- 843 25. M. Ebbo, A. Crinier, F. Vely, E. Vivier, Innate lymphoid cells: major players in inflammatory  
844 diseases. *Nat Rev Immunol* **17**, 665-678 (2017).

- 845 26. P. Licona-Limon, L. K. Kim, N. W. Palm, R. A. Flavell, TH2, allergy and group 2 innate lymphoid  
846 cells. *Nat Immunol* **14**, 536-542 (2013).
- 847 27. K. Moro, T. Yamada, M. Tanabe, T. Takeuchi, T. Ikawa, H. Kawamoto, J. Furusawa, M. Ohtani,  
848 H. Fujii, S. Koyasu, Innate production of T(H)2 cytokines by adipose tissue-associated c-  
849 Kit(+)/Sca-1(+) lymphoid cells. *Nature* **463**, 540-544 (2010).
- 850 28. D. R. Neill, S. H. Wong, A. Bellosi, R. J. Flynn, M. Daly, T. K. Langford, C. Bucks, C. M. Kane, P.  
851 G. Fallon, R. Pannell, H. E. Jolin, A. N. McKenzie, Nuocytes represent a new innate effector  
852 leukocyte that mediates type-2 immunity. *Nature* **464**, 1367-1370 (2010).
- 853 29. A. E. Price, H. E. Liang, B. M. Sullivan, R. L. Reinhardt, C. J. Eisle, D. J. Erle, R. M. Locksley,  
854 Systemically dispersed innate IL-13-expressing cells in type 2 immunity. *Proc Natl Acad Sci U S*  
855 *A* **107**, 11489-11494 (2010).
- 856 30. T. A. Doherty, N. Khorram, S. Lund, A. K. Mehta, M. Croft, D. H. Broide, Lung type 2 innate  
857 lymphoid cells express cysteinyl leukotriene receptor 1, which regulates TH2 cytokine  
858 production. *J Allergy Clin Immunol* **132**, 205-213 (2013).
- 859 31. E. D. Wojno, L. A. Monticelli, S. V. Tran, T. Alenghat, L. C. Osborne, J. J. Thome, C. Willis, A.  
860 Budelsky, D. L. Farber, D. Artis, The prostaglandin D(2) receptor CRTH2 regulates accumulation  
861 of group 2 innate lymphoid cells in the inflamed lung. *Mucosal Immunol* **8**, 1313-1323 (2015).
- 862 32. W. Zhou, S. Toki, J. Zhang, K. Goleniewska, D. C. Newcomb, J. Y. Cephus, D. E. Dulek, M. H.  
863 Bloodworth, M. T. Stier, V. Polosuhkin, R. D. Gangula, S. A. Mallal, D. H. Broide, R. S. Peebles,  
864 Jr., Prostaglandin I2 Signaling and Inhibition of Group 2 Innate Lymphoid Cell Responses. *Am*  
865 *J Respir Crit Care Med* **193**, 31-42 (2016).
- 866 33. J. Maric, A. Ravindran, L. Mazzurana, A. K. Bjorklund, A. Van Acker, A. Rao, D. Friberg, S. E.  
867 Dahlen, A. Heinemann, V. Konya, J. Mjosberg, Prostaglandin E2 suppresses human group 2  
868 innate lymphoid cell function. *J Allergy Clin Immunol* **141**, 1761-1773 e1766 (2018).
- 869 34. L. Denney, A. J. Byrne, T. J. Shea, J. S. Buckley, J. E. Pease, G. M. Herledan, S. A. Walker, L. G.  
870 Gregory, C. M. Lloyd, Pulmonary Epithelial Cell-Derived Cytokine TGF-beta1 Is a Critical  
871 Cofactor for Enhanced Innate Lymphoid Cell Function. *Immunity* **43**, 945-958 (2015).
- 872 35. T. Lammermann, R. N. Germain, The multiple faces of leukocyte interstitial migration. *Semin*  
873 *Immunopathol* **36**, 227-251 (2014).
- 874 36. M. H. Kim, E. J. Taparowsky, C. H. Kim, Retinoic Acid Differentially Regulates the Migration of  
875 Innate Lymphoid Cell Subsets to the Gut. *Immunity* **43**, 107-119 (2015).
- 876 37. M. Salimi, J. L. Barlow, S. P. Saunders, L. Xue, D. Gutowska-Owsiak, X. Wang, L. C. Huang, D.  
877 Johnson, S. T. Scanlon, A. N. McKenzie, P. G. Fallon, G. S. Ogg, A role for IL-25 and IL-33-driven  
878 type-2 innate lymphoid cells in atopic dermatitis. *J Exp Med* **210**, 2939-2950 (2013).
- 879 38. B. Roediger, R. Kyle, K. H. Yip, N. Sumaria, T. V. Guy, B. S. Kim, A. J. Mitchell, S. S. Tay, R. Jain,  
880 E. Forbes-Blom, X. Chen, P. L. Tong, H. A. Bolton, D. Artis, W. E. Paul, B. Fazekas de St Groth,  
881 M. A. Grimbaldston, G. Le Gros, W. Weninger, Cutaneous immunosurveillance and regulation  
882 of inflammation by group 2 innate lymphoid cells. *Nat Immunol* **14**, 564-573 (2013).
- 883 39. M. R. Karta, P. S. Rosenthal, A. Beppu, C. Y. Vuong, M. Miller, S. Das, R. C. Kurten, T. A. Doherty,  
884 D. H. Broide, beta2 integrins rather than beta1 integrins mediate Alternaria-induced group 2  
885 innate lymphoid cell trafficking to the lung. *J Allergy Clin Immunol*, (2017).
- 886 40. R. R. Ricardo-Gonzalez, S. J. Van Dyken, C. Schneider, J. Lee, J. C. Nussbaum, H. E. Liang, D.  
887 Vaka, W. L. Eckalbar, A. B. Molofsky, D. J. Erle, R. M. Locksley, Tissue signals imprint ILC2  
888 identity with anticipatory function. *Nat Immunol*, (2018).
- 889 41. M. F. Krummel, F. Bartumeus, A. Gerard, T cell migration, search strategies and mechanisms.  
890 *Nat Rev Immunol* **16**, 193-201 (2016).
- 891 42. Y. Kondo, T. Yoshimoto, K. Yasuda, S. Futatsugi-Yumikura, M. Morimoto, N. Hayashi, T.  
892 Hoshino, J. Fujimoto, K. Nakanishi, Administration of IL-33 induces airway  
893 hyperresponsiveness and goblet cell hyperplasia in the lungs in the absence of adaptive  
894 immune system. *Int Immunol* **20**, 791-800 (2008).

- 895 43. S. Boitano, A. N. Flynn, C. L. Sherwood, S. M. Schulz, J. Hoffman, I. Gruzina, M. O. Daines,  
896 *Alternaria alternata* serine proteases induce lung inflammation and airway epithelial cell  
897 activation via PAR2. *Am J Physiol Lung Cell Mol Physiol* **300**, L605-614 (2011).
- 898 44. M. B. Headley, A. Bins, A. Nip, E. W. Roberts, M. R. Looney, A. Gerard, M. F. Krummel,  
899 Visualization of immediate immune responses to pioneer metastatic cells in the lung. *Nature*  
900 **531**, 513-517 (2016).
- 901 45. M. A. Schaller, L. E. Kallal, N. W. Lukacs, A key role for CC chemokine receptor 1 in T-cell-  
902 mediated respiratory inflammation. *Am J Pathol* **172**, 386-394 (2008).
- 903 46. S. A. Islam, D. S. Chang, R. A. Colvin, M. H. Byrne, M. L. McCully, B. Moser, S. A. Lira, I. F. Charo,  
904 A. D. Luster, Mouse CCL8, a CCR8 agonist, promotes atopic dermatitis by recruiting IL-5+ T(H)2  
905 cells. *Nat Immunol* **12**, 167-177 (2011).
- 906 47. W. Xu, J. P. Di Santo, Taming the beast within: regulation of innate lymphoid cell homeostasis  
907 and function. *J Immunol* **191**, 4489-4496 (2013).
- 908 48. L. Xue, M. Salimi, I. Panse, J. M. Mjosberg, A. N. McKenzie, H. Spits, P. Klenerman, G. Ogg,  
909 Prostaglandin D2 activates group 2 innate lymphoid cells through chemoattractant receptor-  
910 homologous molecule expressed on TH2 cells. *J Allergy Clin Immunol* **133**, 1184-1194 (2014).
- 911 49. L. G. Gregory, S. A. Mathie, S. A. Walker, S. Pegorier, C. P. Jones, C. M. Lloyd, Overexpression  
912 of Smad2 drives house dust mite-mediated airway remodeling and airway  
913 hyperresponsiveness via activin and IL-25. *Am J Respir Crit Care Med* **182**, 143-154 (2010).
- 914 50. G. J. Laurent, Lung collagen: more than scaffolding. *Thorax* **41**, 418-428 (1986).
- 915 51. A. Andersson-Sjoland, O. Hallgren, S. Rolandsson, M. Weitoft, E. Tykesson, A. K. Larsson-  
916 Callerfelt, K. Rydell-Tormanen, L. Bjermer, A. Malmstrom, J. C. Karlsson, G. Westergren-  
917 Thorsson, Versican in inflammation and tissue remodeling: the impact on lung disorders.  
918 *Glycobiology* **25**, 243-251 (2015).
- 919 52. R. Cicchi, D. Kapsokalyvas, V. De Giorgi, V. Maio, A. Van Wiechen, D. Massi, T. Lotti, F. S.  
920 Pavone, Scoring of collagen organization in healthy and diseased human dermis by  
921 multiphoton microscopy. *J Biophotonics* **3**, 34-43 (2010).
- 922 53. C. Vennin, V. T. Chin, S. C. Warren, M. C. Lucas, D. Herrmann, A. Magenau, P. Melenec, S. N.  
923 Walters, G. Del Monte-Nieto, J. R. Conway, M. Nobis, A. H. Allam, R. A. McCloy, N. Currey, M.  
924 Pinese, A. Boulghourjian, A. Zaratzian, A. A. Adam, C. Heu, A. M. Nagrial, A. Chou, A.  
925 Steinmann, A. Drury, D. Froio, M. Giry-Laterriere, N. L. Harris, T. Phan, R. Jain, W. Weninger,  
926 E. J. McGhee, R. Whan, A. L. Johns, J. S. Samra, L. Chantrill, A. J. Gill, M. Kohonen-Corish, R. P.  
927 Harvey, A. V. Biankin, I. Australian Pancreatic Cancer Genome, T. R. Evans, K. I. Anderson, S. T.  
928 Grey, C. J. Ormandy, D. Gallego-Ortega, Y. Wang, M. S. Samuel, O. J. Sansom, A. Burgess, T. R.  
929 Cox, J. P. Morton, M. Pajic, P. Timpson, Transient tissue priming via ROCK inhibition uncouples  
930 pancreatic cancer progression, sensitivity to chemotherapy, and metastasis. *Sci Transl Med* **9**,  
931 (2017).
- 932 54. A. Leithner, A. Eichner, J. Muller, A. Reversat, M. Brown, J. Schwarz, J. Merrin, D. J. de Gorter,  
933 F. Schur, J. Bayerl, I. de Vries, S. Wieser, R. Hauschild, F. P. Lai, M. Moser, D. Kerjaschki, K.  
934 Rottner, J. V. Small, T. E. Stradal, M. Sixt, Diversified actin protrusions promote environmental  
935 exploration but are dispensable for locomotion of leukocytes. *Nat Cell Biol* **18**, 1253-1259  
936 (2016).
- 937 55. P. Friedl, S. Borgmann, E. B. Brocker, Amoeboid leukocyte crawling through extracellular  
938 matrix: lessons from the Dictyostelium paradigm of cell movement. *J Leukoc Biol* **70**, 491-509  
939 (2001).
- 940 56. T. Lammermann, M. Sixt, Mechanical modes of 'amoeboid' cell migration. *Curr Opin Cell Biol*  
941 **21**, 636-644 (2009).
- 942 57. N. J. Kenyon, R. W. Ward, G. McGrew, J. A. Last, TGF-beta1 causes airway fibrosis and  
943 increased collagen I and III mRNA in mice. *Thorax* **58**, 772-777 (2003).

- 944 58. T. Honda, J. G. Egen, T. Lammermann, W. Kastentmuller, P. Torabi-Parizi, R. N. Germain, Tuning  
945 of antigen sensitivity by T cell receptor-dependent negative feedback controls T cell effector  
946 function in inflamed tissues. *Immunity* **40**, 235-247 (2014).
- 947 59. M. T. Stier, J. Zhang, K. Goleniewska, J. Y. Cephus, M. Rusznak, L. Wu, L. Van Kaer, B. Zhou, D.  
948 C. Newcomb, R. S. Peebles, Jr., IL-33 promotes the egress of group 2 innate lymphoid cells  
949 from the bone marrow. *J Exp Med*, (2017).
- 950 60. R. Sumagin, H. Prizant, E. Lomakina, R. E. Waugh, I. H. Sarelius, LFA-1 and Mac-1 define  
951 characteristically different intraluminal crawling and emigration patterns for monocytes and  
952 neutrophils in situ. *J Immunol* **185**, 7057-7066 (2010).
- 953 61. J. von Moltke, M. Pepper, Sentinels of the Type 2 Immune Response. *Trends Immunol*, (2017).
- 954 62. S. A. Islam, A. D. Luster, T cell homing to epithelial barriers in allergic disease. *Nat Med* **18**,  
955 705-715 (2012).
- 956 63. M. Barczyk, S. Carracedo, D. Gullberg, Integrins. *Cell Tissue Res* **339**, 269-280 (2010).
- 957 64. J. F. Moreau, T. Pradeu, A. Grignolio, C. Nardini, F. Castiglione, P. Tieri, M. Capri, S. Salvioli, J.  
958 L. Taupin, P. Garagnani, C. Franceschi, The emerging role of ECM crosslinking in T cell mobility  
959 as a hallmark of immunosenescence in humans. *Ageing Res Rev* **35**, 322-335 (2017).
- 960 65. G. Burgstaller, S. Vierkotten, M. Lindner, M. Konigshoff, O. Eickelberg, Multidimensional  
961 immunolabeling and 4D time-lapse imaging of vital ex vivo lung tissue. *Am J Physiol Lung Cell*  
962 *Mol Physiol* **309**, L323-332 (2015).
- 963 66. M. R. Looney, E. E. Thornton, D. Sen, W. J. Lamm, R. W. Glenny, M. F. Krummel, Stabilized  
964 imaging of immune surveillance in the mouse lung. *Nat Methods* **8**, 91-96 (2011).
- 965 67. B. W. Miller, J. P. Morton, M. Pinese, G. Saturno, N. B. Jamieson, E. McGhee, P. Timpson, J.  
966 Leach, L. McGarry, E. Shanks, P. Bailey, D. Chang, K. Oien, S. Karim, A. Au, C. Steele, C. R. Carter,  
967 C. McKay, K. Anderson, T. R. Evans, R. Marais, C. Springer, A. Biankin, J. T. Erler, O. J. Sansom,  
968 Targeting the LOX/hypoxia axis reverses many of the features that make pancreatic cancer  
969 deadly: inhibition of LOX abrogates metastasis and enhances drug efficacy. *EMBO Mol Med* **7**,  
970 1063-1076 (2015).
- 971 68. N. Rath, J. P. Morton, L. Julian, L. Helbig, S. Kadir, E. J. McGhee, K. I. Anderson, G. Kalna, M.  
972 Mullin, A. V. Pinho, I. Rooman, M. S. Samuel, M. F. Olson, ROCK signaling promotes collagen  
973 remodeling to facilitate invasive pancreatic ductal adenocarcinoma tumor cell growth. *EMBO*  
974 *Mol Med* **9**, 198-218 (2017).
- 975 69. D. O. Villarreal, A. L'Huillier, S. Armington, C. Mottershead, E. V. Filippova, B. D. Coder, R. G.  
976 Petit, M. F. Princiotta, Targeting CCR8 Induces Protective Antitumor Immunity and Enhances  
977 Vaccine-Induced Responses in Colon Cancer. *Cancer Res* **78**, 5340-5348 (2018).
- 978 70. T. Cheng, Q. Liu, R. Zhang, Y. Zhang, J. Chen, R. Yu, G. Ge, Lysyl oxidase promotes bleomycin-  
979 induced lung fibrosis through modulating inflammation. *J Mol Cell Biol* **6**, 506-515 (2014).

980

## 981 **Acknowledgements**

982 The authors thank Stephen Rothery, David Gaboriau and Andreas Bruckbauer from the FILM  
983 facility (in part funded by Wellcome Trust grant 104931/Z/14/Z), members of the Beatson  
984 Advanced Imaging Resource (BAIR) team for excellent technical and imaging assistance. We  
985 would additionally like to thank Jane Srivastava and Jessica Rowley, of the Imperial College  
986 Core Flow Cytometry facility for assistance with flow cytometry and Lorraine Lawrence for  
987 histological sectioning. We would additionally like to thank, Dhiren Patel, Helen Stoelting, Nuo  
988 En Chan and Megan Mc Fie for their expert technical assistance. We would additionally like

989 to acknowledge Lucy Robson for thorough maintenance of the human ILC2 lines. Finally, we  
990 would like to acknowledge MotilityLab for providing the resource for carrying out our analysis  
991 on ILC2 dynamics.

992

### 993 **Funding**

994 L.M.C. thanks the MRC (MR/M01245X/1) and Cancer Research UK for funding (Institute  
995 group funding ref 23983). This study was funded by the Wellcome Trust grant 107059/Z/15/Z,  
996 awarded to C.M.L. who is a Wellcome Senior Fellow in Basic Biomedical Sciences.

997

### 998 **Author Contributions**

999 C.M.L. conceived the idea and directed the study. L.M.C. provided expertise in imaging  
1000 techniques. J.E.P. provided expert advice on chemotaxis assays. M. B. H. and M.F.K provided  
1001 expert advice on intravital imaging. F.P., L.D., L.G.G., L.M.C. and C.M.L. wrote the manuscript.  
1002 F.P. L.D. designed the experiments and F.P., L.D., L.J.E., L.M.C., J.V., R.O. performed  
1003 experiments. F.P., E.J.M., L.M.C and L.D. analysed the data. F.P., E.J.M., L.M.C. and L.D.  
1004 generated figures. R.O. maintained and genotyped the mouse lines.

1005

### 1006 **Competing Interests**

1007 The authors declare that they have no competing interest.

### 1008 **Main text figure legends:**

1009 **Fig 1. The number of ILC2 rapidly increase in the peribronchial / perivascular region**  
1010 **after rIL-33 treatment.** IL13-eGFP mice were treated with 3 doses of rIL-33 (1µg per dose),  
1011 Alt (10µg) or PBS (25µl) over 1 week and culled 24h after the final dose. The frequency of  
1012 ILC2 (GFP<sup>+</sup>CD45<sup>+</sup>Lin<sup>neg</sup>CD3<sup>-</sup>NKp46<sup>-</sup>CD127<sup>+</sup>CD90.2<sup>+</sup>KLRG1<sup>+</sup>CD25<sup>var</sup>IL-13<sup>+</sup>IL-5<sup>+</sup>) in the **(A)**  
1013 airways (BAL fluid), **(B)** lung and **(C)** lung draining lymph nodes (mediastinal). Live viable  
1014 precision cut lung slices of 200µm thickness were obtained and stained for CD31 (Magenta,  
1015 the lung structure and blood vessels), CD4 (cyan, T cells, orange arrow), EpCAM (Red, to

1016 visualise bronchial epithelium) and GFP (ILC2, white arrow). Images of 1024 $\mu$ m x 1024 $\mu$ m  
1017 field of view (FOV) were taken under a 20x objective using an inverted confocal microscope.  
1018 **(D)** Images showing ILC2 (GFP<sup>+</sup>CD4<sup>-</sup>) CD4<sup>+</sup> T cells (CD4<sup>+</sup>GFP<sup>-</sup>) location in PBS, rIL-33 and  
1019 Alt treated mice, scale bar, 150  $\mu$ m. **(E)** Number of ILC2 (GFP<sup>+</sup>CD4<sup>-</sup>) in lung sections per FOV  
1020 taken under a 10x objective. **(F)** Schematic illustration of the lung depicting the anatomical  
1021 location in the lung where precision cut lung slices were prepared. Representative images  
1022 show two regions of the lung slice from a rIL-33 treated mouse showing distribution of ILC2  
1023 and CD4<sup>+</sup> T cells, scale bar 150  $\mu$ m. n = 4 mice per group (Mock(PBS)), n= 6 mice per group  
1024 (Alt or rIL-33 treatment). Data representative of 4 experiments. \*p < 0.05, \*\*p < 0.01, \*\*\*p <  
1025 0.001\_and, \*\*\*\* p < 0.0001.

1026

1027 **Fig 2. rIL-33 stimulation induces ILC2 motility around blood vessels and airways.** IL13-  
1028 eGFP mice were treated with 3 doses of rIL-33 (1 $\mu$ g per dose), over 1 week and culled 24h  
1029 after the final dose. Live viable precision cut lung slices (PCLS) of 200 $\mu$ m thickness were  
1030 obtained and stained for CD31 (Magenta, the lung structure and blood vessels), CD4 (cyan,  
1031 T cells, orange arrow), EpCAM (Red, to visualise bronchial epithelium) and GFP (ILC2, white  
1032 arrow), and time-lapse video taken (1024 $\mu$ m x 1024 $\mu$ m field of view (FOV), 45 min duration  
1033 under a 20x objective using an inverted confocal microscope) **(A)** Static image depicting the  
1034 location of ILC2 and CD4<sup>+</sup> T cells, scale bar 100  $\mu$ m. **(B)** Zoomed in section of the blood vessel  
1035 in figure 2A, scale bar 20  $\mu$ m. **(C)** High power images of boxed cells in figure 2B showing  
1036 differences in pattern of cell movement (oscillatory vs amoeboid movement). ILC2 and CD4<sup>+</sup>  
1037 T cells dynamics were tracked and plotted as **(D)** individual tracks or **(E)** tracks commencing  
1038 from centroid and overlaid. **(F)** Track speed, **(G)** track length and **(H)** track displacement were  
1039 quantified. Representative images shown in **(A-C)** are from rIL-33 treated mice, where n = 6  
1040 mice per treatment (3 slices per mouse were imaged). For **(F-H)** in box and whiskers plots,

1041 each dot represents an individual cell. Data are representative from 4 experiments where n =  
1042 6 mice per treatment. \*p < 0.05, \*\*p < 0.01, \*\*\*p < 0.001\_and, \*\*\*\* p < 0.0001.

1043

1044 **Fig 3. rIL-33 stimulation induces ILC2 motility around blood vessels and airways.** IL13-  
1045 eGFP mice were treated with 3 doses of rIL-33 (1µg per dose) or Alt (10µg) over 1 week. Live  
1046 precision cut lung slices were obtained and ILC2 dynamics were compared between the two  
1047 and the differences were plotted as **(A)** individual tracks and **(B)** tracks commencing from  
1048 centroid and overlaid. Differences in tracks between treatments were quantified as **(C)** track  
1049 speed, **(D)** track length and **(E)** track displacement. Intravital microscopy (IVM) was performed  
1050 in live IL-13eGFP mice after rIL-33 treatment (one 512µm x 512µm field of view (FOV) in a 1-  
1051 hour-duration video). **(F)** Static images of different frames captured during the course of the  
1052 video depicting amoeboid shape changes of ILC2 at separate time-points, scale bar 20 µm. n  
1053 ≥ 4 mice per group. Data representative of 4 experiments. \*p < 0.05, \*\*p < 0.01, \*\*\*p < 0.001  
1054 and, \*\*\*\* p < 0.0001. Quantifications from **(A-E)** are representative of 4 experiments, where  
1055 n = 6 mice per treatment (3 slices per mouse were imaged). For **(F)** IVM images are  
1056 representative of 6 individual IL-33 treated mice. \*p < 0.05, \*\*p < 0.01, \*\*\*p < 0.001\_and, \*\*\*\* p  
1057 < 0.0001.

1058

1059 **Fig 4. ILC2 utilize distinct chemotactic pathways to home to inflammatory sites in the**  
1060 **lung.** IL13-eGFP mice were treated with 3 doses of rIL-33 (1µg per dose) or PBS (25µl), over  
1061 1 week and culled 24h after the final dose. **(A)** The percentage of murine ILC2  
1062 (CD45<sup>+</sup>Lin<sup>neg</sup>NKp46<sup>-</sup>CD3<sup>-</sup>) expressing CCR1, CCR4 and CCR8. CCL8 levels in murine **(B)**  
1063 BAL and **(C)** lung. **(D)** Location of CCL8 expression and ILC2 and **(E)** quantified CCL8  
1064 deposits in PCLS stained for CD31 (Magenta, the lung structure and blood vessels), CCL8  
1065 (cyan, yellow arrow), EpCAM (Red, to visualise bronchial epithelium) and GFP (ILC2, white  
1066 arrow), images of 1024µm x 1024µm FOV, scale bar 150 µm. Human ILC2 lines were  
1067 generated and migration to varying concentrations of **(F)** PGD<sub>2</sub> and **(G)** CCL8 were

1068 determined. **(H)** Peak migratory responses of a human ILC2 cell line to IL-25, TGF- $\beta$ , rIL-33,  
1069 CCL8 and PGD<sub>2</sub>. IL13-eGFP mice treated with rIL-33 were also treated with 5 $\mu$ g purified anti-  
1070 mouse CCR8 antibody i.p., rCCL8 i.n. or an isotype control and PCLS obtained and stained.  
1071 **(I)** Localisation of ILC2 in live PCLS. **(J)** Number of ILC2 per FOV under 10x objective. Time-  
1072 lapse imaging of 45 min duration was performed and ILC2 **(K)** track from centroid, **(L)** track  
1073 length and **(M)** track speed and **(N)** track displacement were quantified. In box and whiskers  
1074 graphs each data point represents an individual cell. Balb/c mice treated with rIL-33 were  
1075 further treated with rCCL8,  $\alpha$ CCR8 or Isotype control antibody. **(O)** Percentage of IL-13<sup>+</sup>IL-5<sup>+</sup>  
1076 ILC2 (CD45<sup>+</sup>lin<sup>-</sup>NKp46<sup>-</sup>CD3<sup>-</sup>GATA-3<sup>+</sup>). **(P)** Representation Histogram of MFI of IL-13 and IL-5  
1077 and quantification of MFI for **(Q)** IL-13 and **(R)** IL-5 from GATA<sup>+</sup> ILC2. For panels **A-E** n  $\geq$  4  
1078 mice per group. Data representative of 4 experiments. For panels **F-H** n = 3 individual donors.  
1079 Data representative of 3 experiments. For panels **I-R**, n = 5 mice per group. Data  
1080 representative of 2 experiments \*p < 0.05, \*\*p < 0.01, \*\*\*p < 0.001 and,\*\*\*\* p < 0.0001.

1081

1082

1083 **Fig 5. Extracellular matrix proteins, collagen-IV and fibronectin, promote increased**  
1084 **ILC2 motility.** Human ILC2 lines were seeded on tissue culture plates coated with either 10%  
1085 FBS, fibronectin, collagen-I, collagen-IV or serum free coating (control) for 24h. Cell movement  
1086 was imaged via the JuLI imaging system and plotted as **(A)** individual tracks, **(B)** track speed  
1087 dot plots and **(C)** track speed spider plot. IL13-eGFP mice were treated with 3 doses of rIL-33  
1088 (1 $\mu$ g per dose) or PBS (25 $\mu$ l), over 1 week and culled 24h after the final dose PCLS obtained.  
1089 **(D)** SHG imaging of PCLS revealing collagen fibres, representative maximum intensity  
1090 projections, scale bar 50 $\mu$ m. **(E)** GLCM analysis of SHG imaging. **(F)** Images of Fibronectin  
1091 expression and localisation. PCLS stained for CD31 (Magenta, the lung structure and blood  
1092 vessels), Fibronectin (cyan, yellow arrow), EpCAM (Red, to visualise bronchial epithelium)  
1093 and GFP (ILC2, white arrow) and images of 1024 $\mu$ m x 1024 $\mu$ m field of view (FOV) were taken,  
1094 scale bar 150 $\mu$ m. For panels **A-C**, n = 3 donors (in triplicate). Data representative of 3



1095 experiments. For panels **D-F** n = 6 (in triplicate). \*p < 0.05, \*\*p < 0.01, \*\*\*p < 0.001 and,\*\*\*\*,  
1096 \*\*\*\* P < 0.0001.

1097

1098

1099 **Fig 6. Collagen-I enhances ILC2 actin cytoskeletal remodelling and polarity.** Human ILC2

1100 lines were seeded on tissue culture plates coated with either 10% FBS, fibronectin, collagen-

1101 I, collagen-IV or serum free coating (control) and imaged after 12 hours. **(A)** Bright field images

1102 depicting change in shape. **(B)** Actin remodelling following staining with Phalloidin (green) and

1103 DAPI (cyan) and imaging using Airyscan detection (maximum intensity projections), scale bar

1104 5µm. **(C)** Cell area. **(D)** Cell perimeter. n = 3 donors. Data representative of 2 experiments. \*\*\*

1105 P < 0.001.

1106

1107 **Fig 7. Blocking collagen fibrillogenesis *in vivo* increases ILC2 dynamics in the inflamed**

1108 **lung.** IL13-eGFP mice treated with rIL-33 were further treated with (BAPN) along with controls

1109 were culled 24 hours after the final dose. ILC2 dynamics from live PCLS were plotted as either

1110 **(A)** individual tracks or **(B)** tracks commencing from centroid and overlaid. Differences in

1111 tracks between treatments were quantified as **(C)** track speed, **(D)** track length and **(E)** track

1112 displacement. Total ILC2 ( ) in **(F)** Lungs, **(G)** BAL and **(H)** Blood were enumerated. For panels

1113 **A-E** n ≥ 4 mice per group. Data representative of 4 experiments. For panels **F-H** n = 6 mice

1114 per group. Data representative of 2 experiments. \* P < 0.05, \*\* P < 0.01, \*\*\* P < 0.001, \*\*\*\* P

1115 < 0.0001.

1116

1117 **Fig 8. Blocking collagen fibrillogenesis reduces eosinophil accumulation in the**

1118 **inflamed lung.** Balb/c mice were treated with rIL-33 or PBS with or without BAPN. **(A)** Airway

1119 responsiveness to methacholine. Lung **(B)** alveolar macrophages (AM), **(C)** dendritic cells

1120 (DC), **(D)** neutrophils and **(E)** were enumerated by flow cytometry. **(F)** CCL24 protein in lung

1121 tissue. **(G)** Congo red stained eosinophils (blue arrow) in lung histological samples. scale bar

1122 50µm **H** Quantification of eosinophil from histological samples. For panels **A-E** n ≥ 6 mice per

1123 group. Data representative of 2 experiments. For panels **G and H**  $n \geq 4$  mice per group. Data  
1124 representative of 2 experiments. \*  $P < 0.05$ , \*\*  $P < 0.01$ , \*\*\*  $P < 0.001$ , \*\*\*\*  $P < 0.0001$ .

1125

1126

1127

1128

1129

1130

1131

1132

1133

1134

1135

1136

1137

1138

1139

1140

1141

1142

1143

1144

1145

1146

1147

1148

1149

1150

1151

1152

1153

1154

# Figure 1

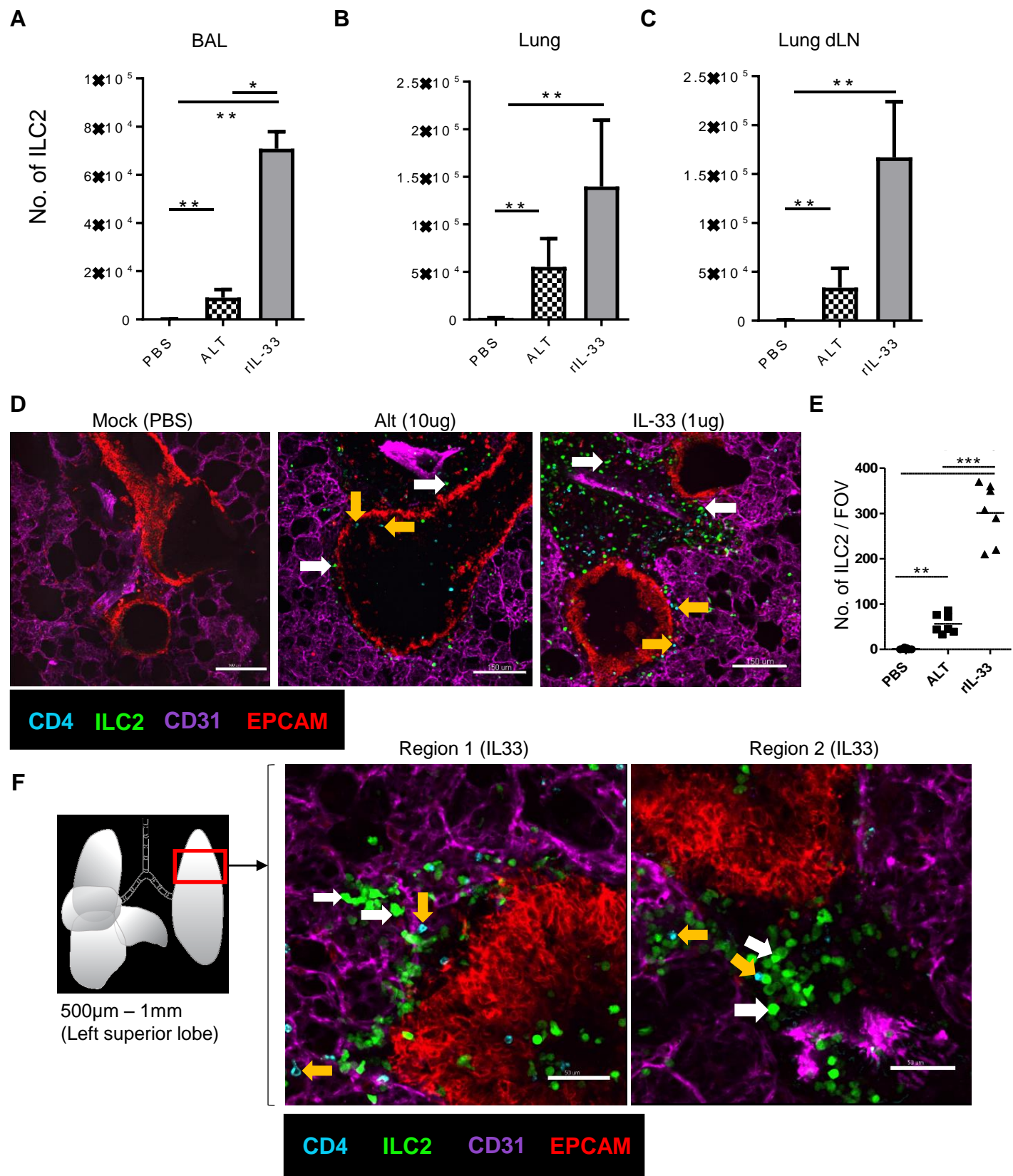


Figure 2

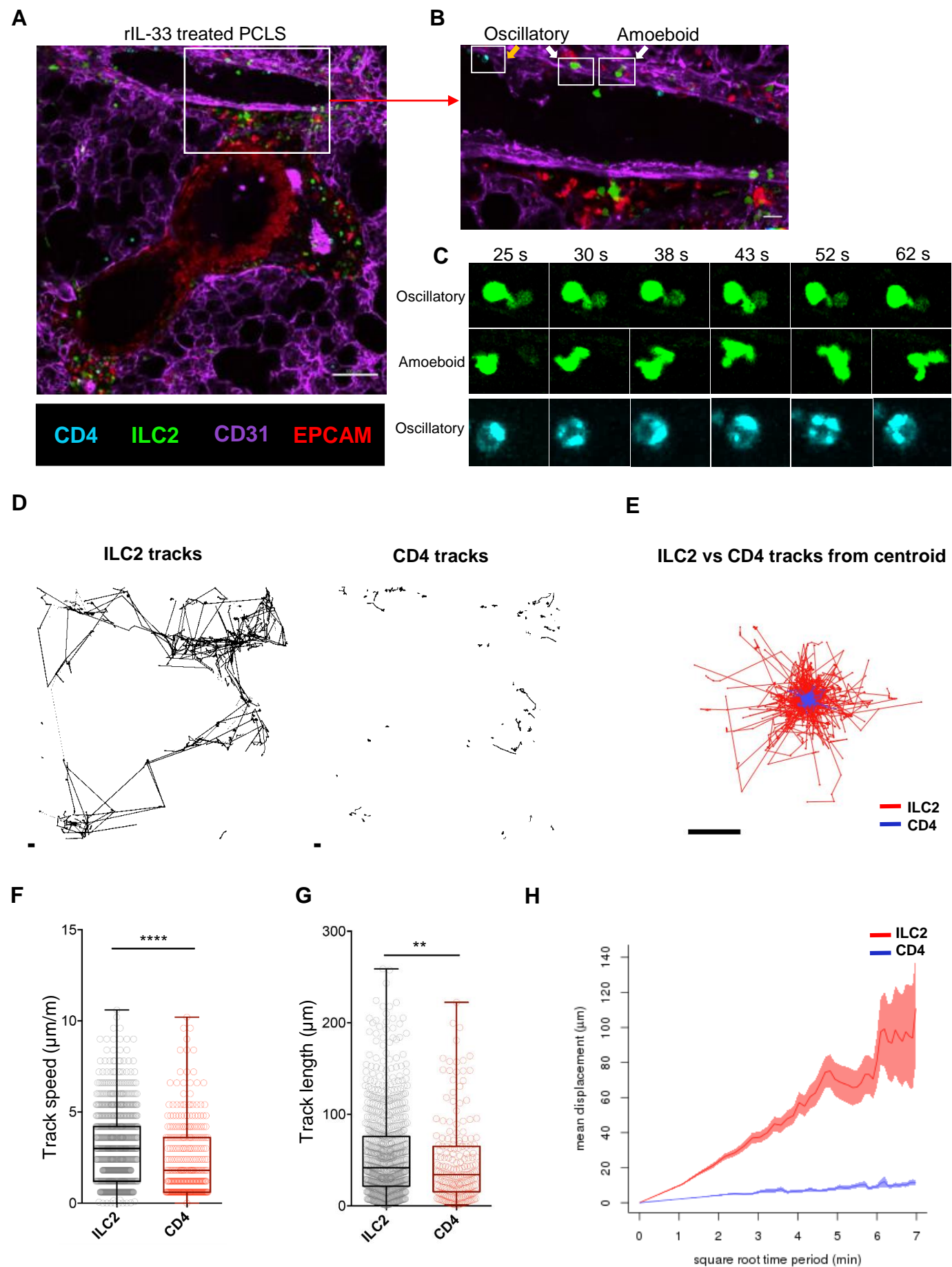
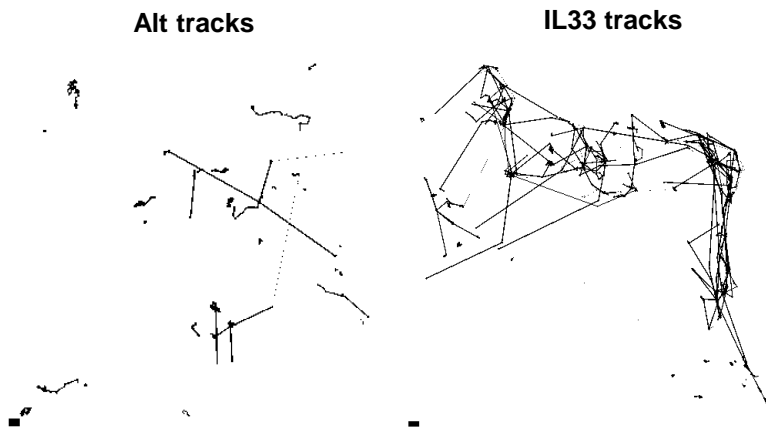
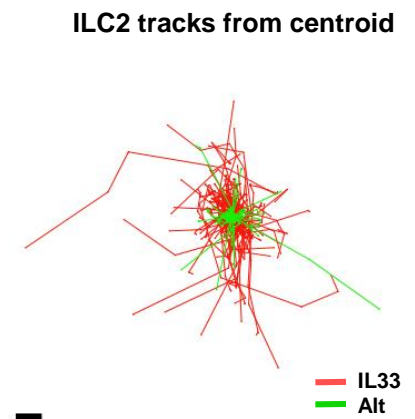


Figure 3

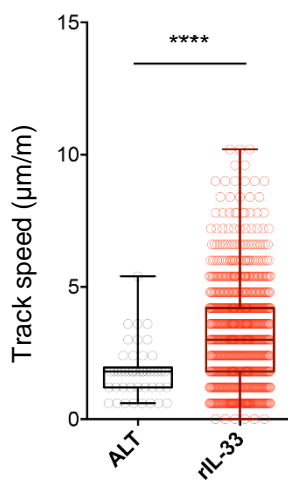
A



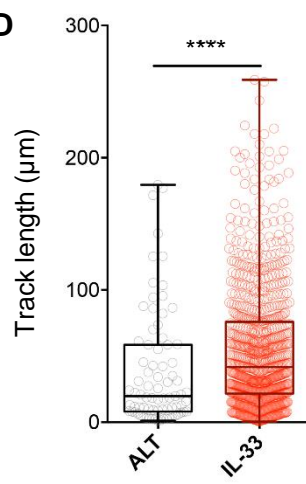
B



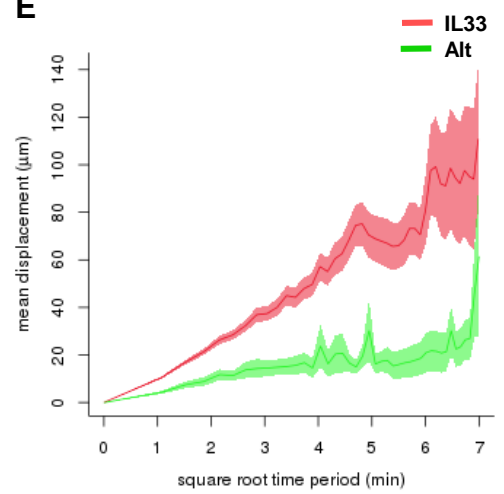
C



D



E



F

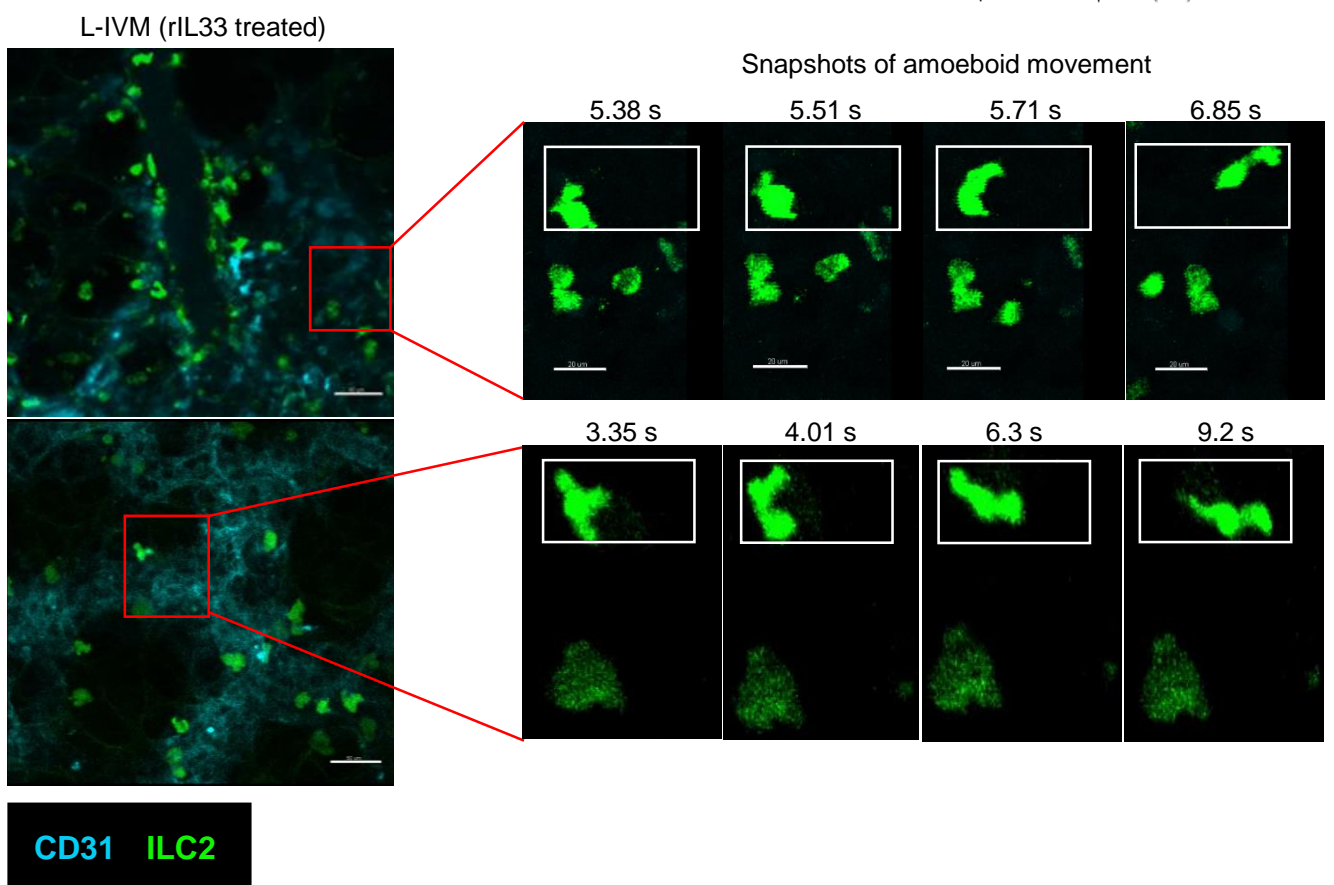


# Figure 4

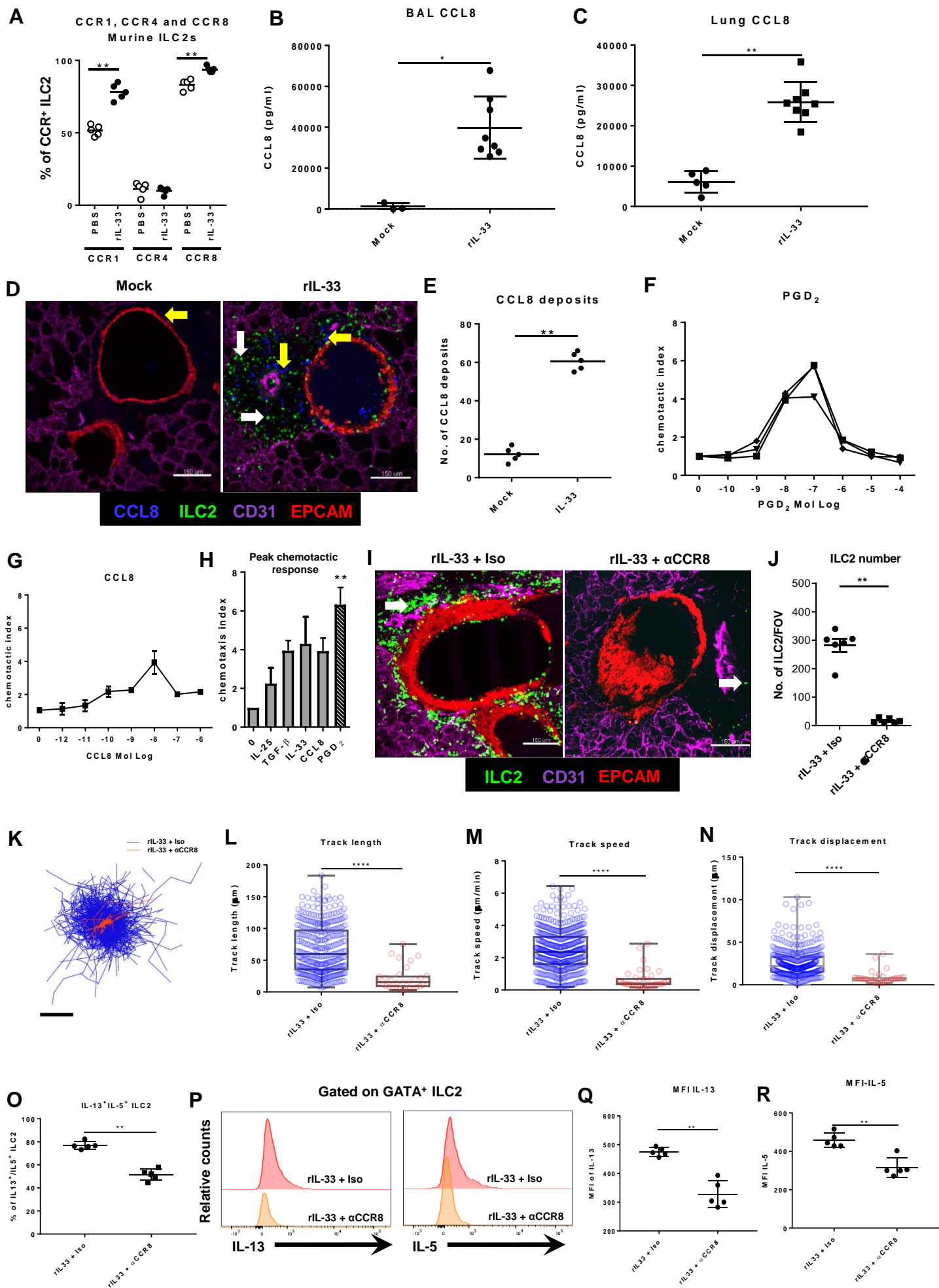


# Figure 5

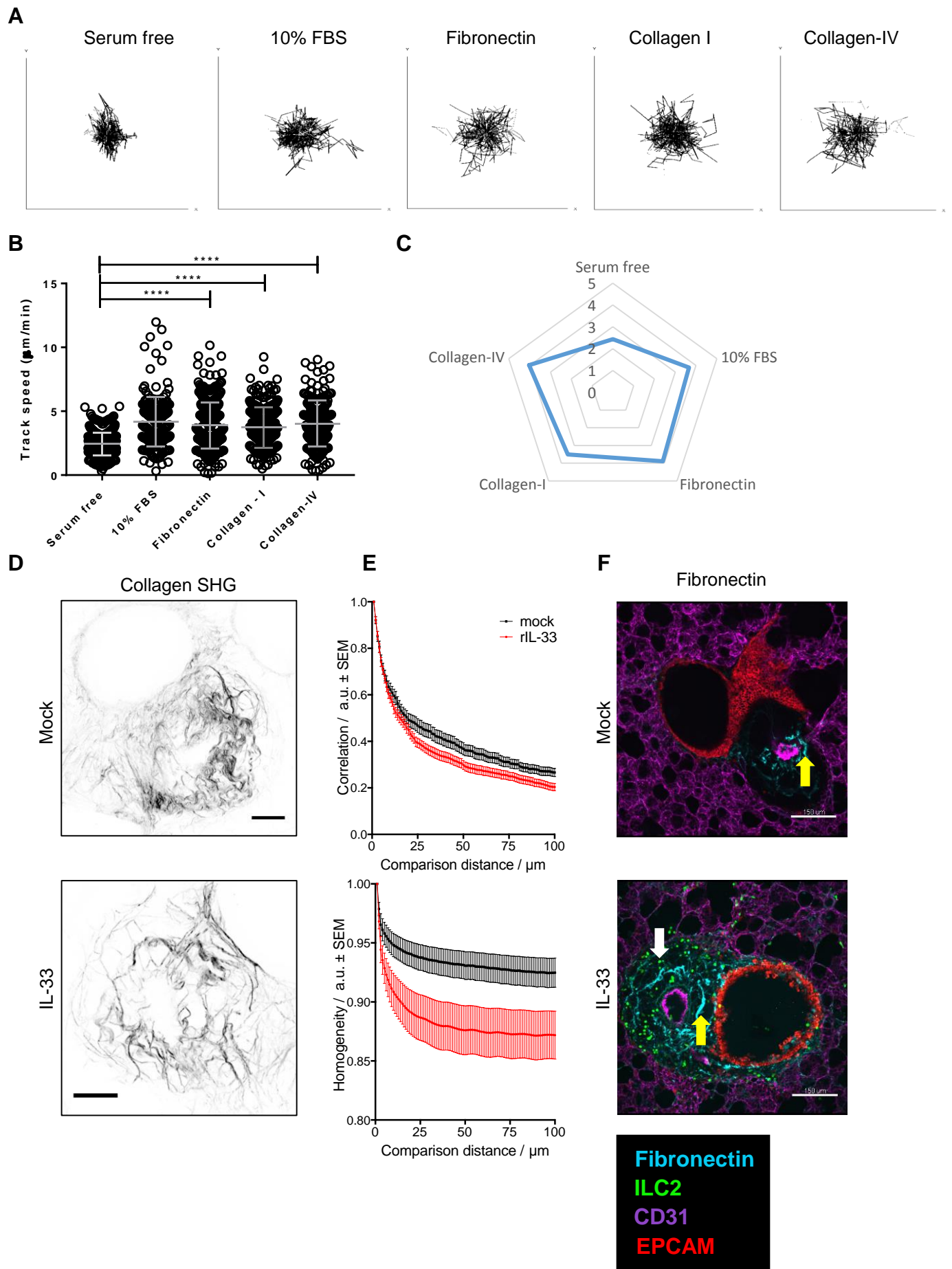


Figure 6

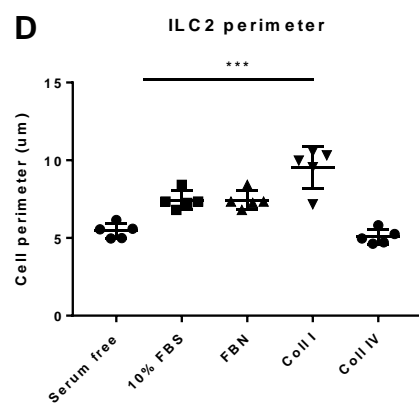
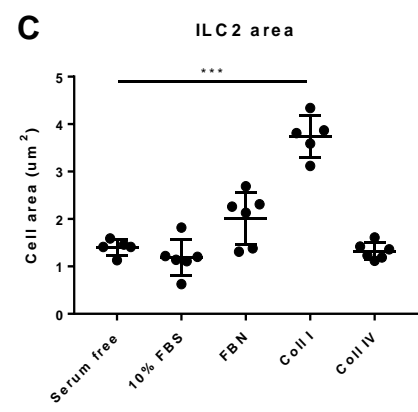
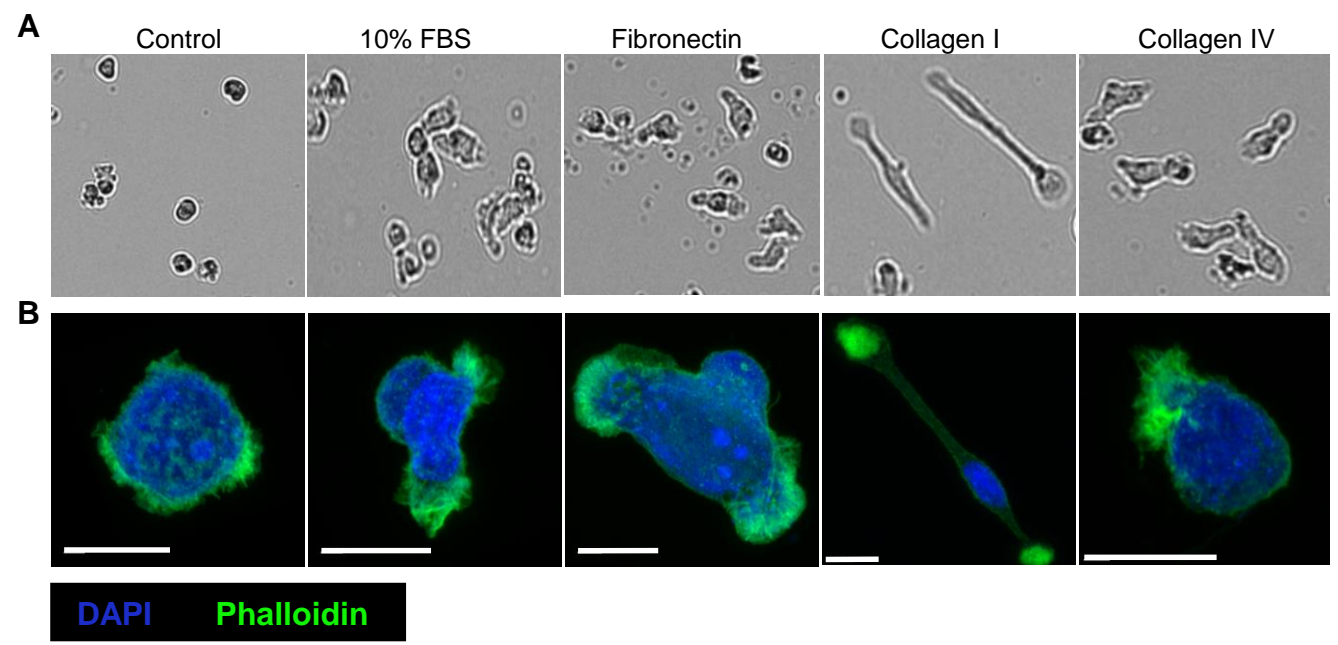




Figure 7

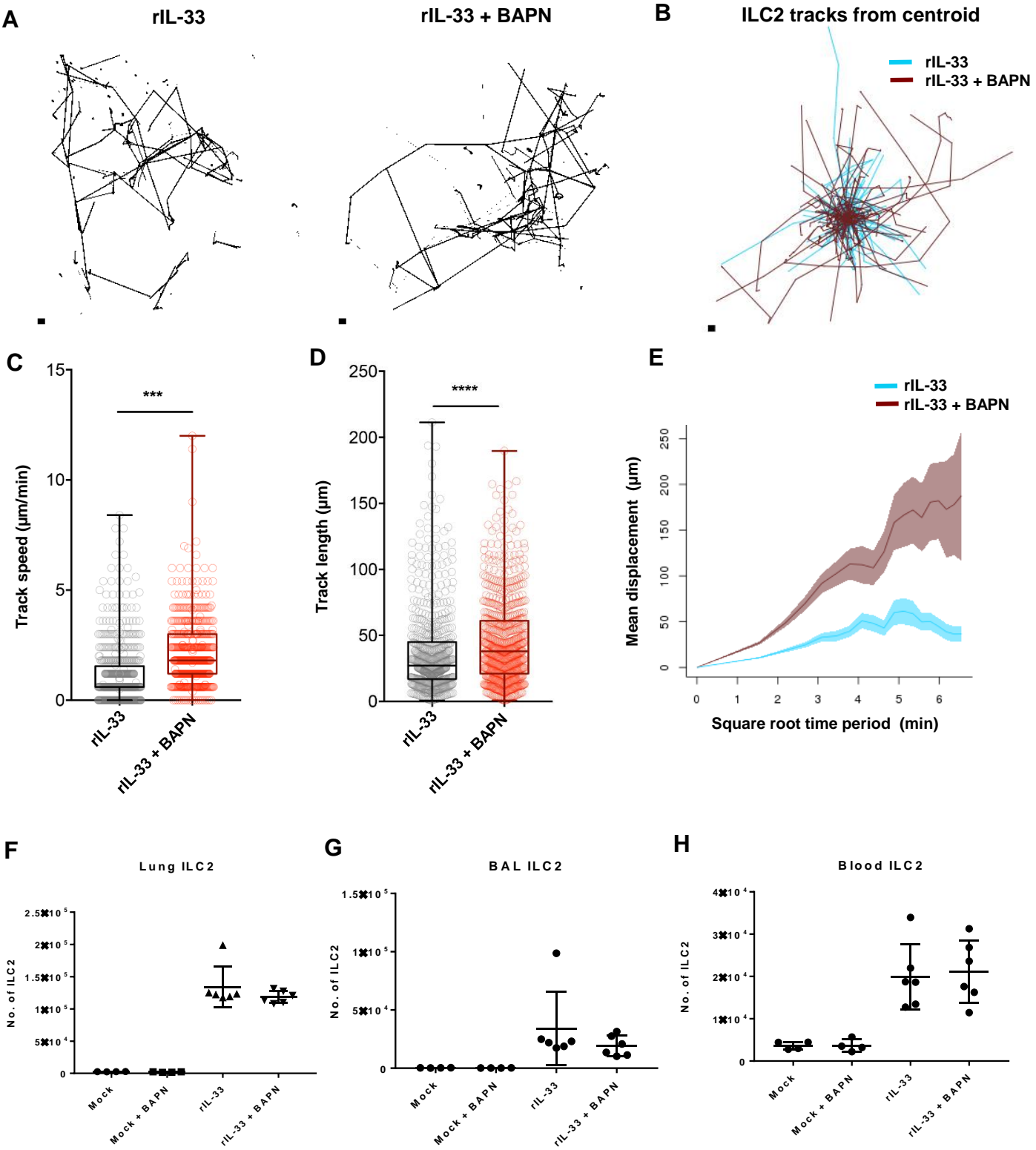
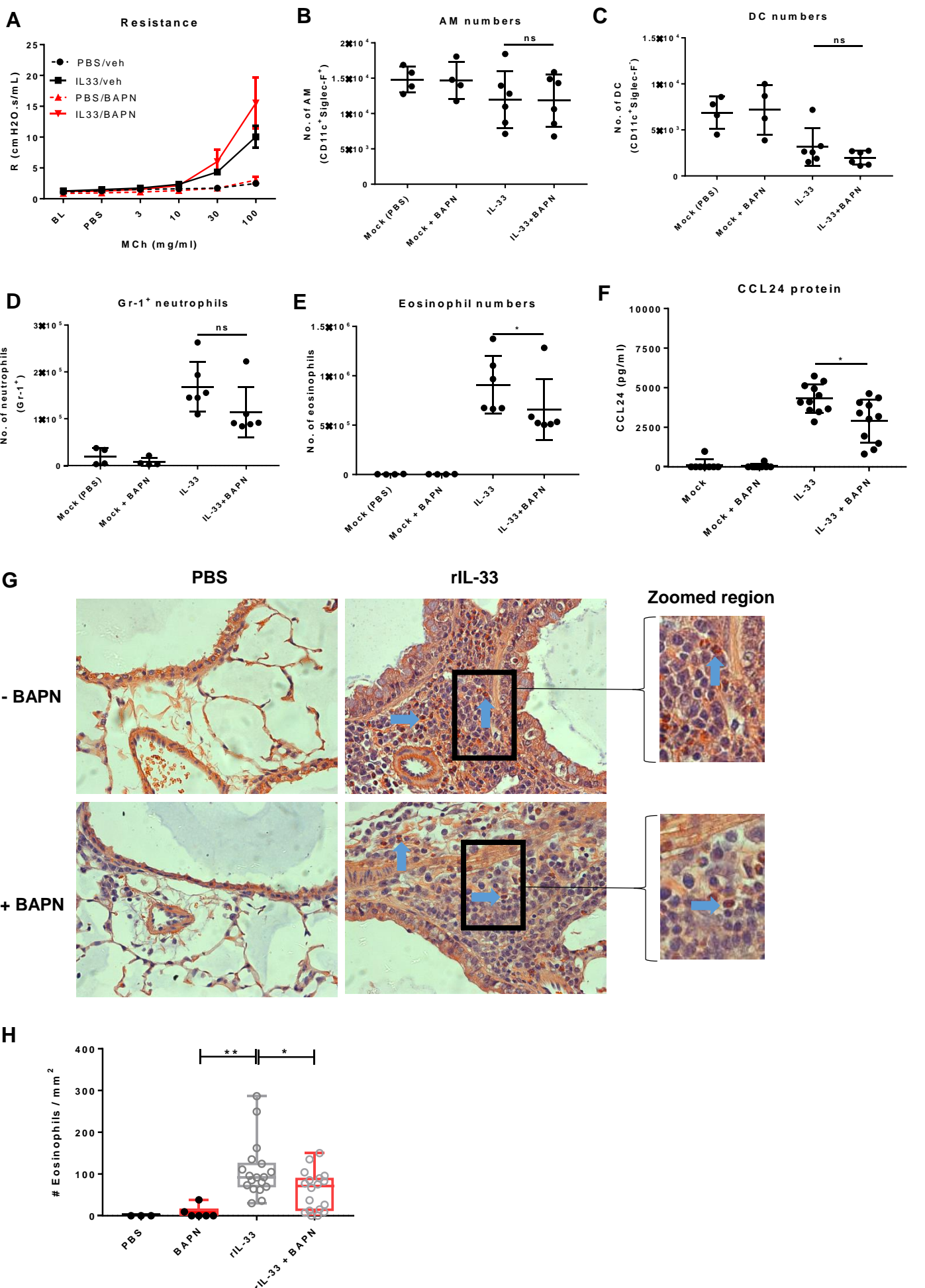
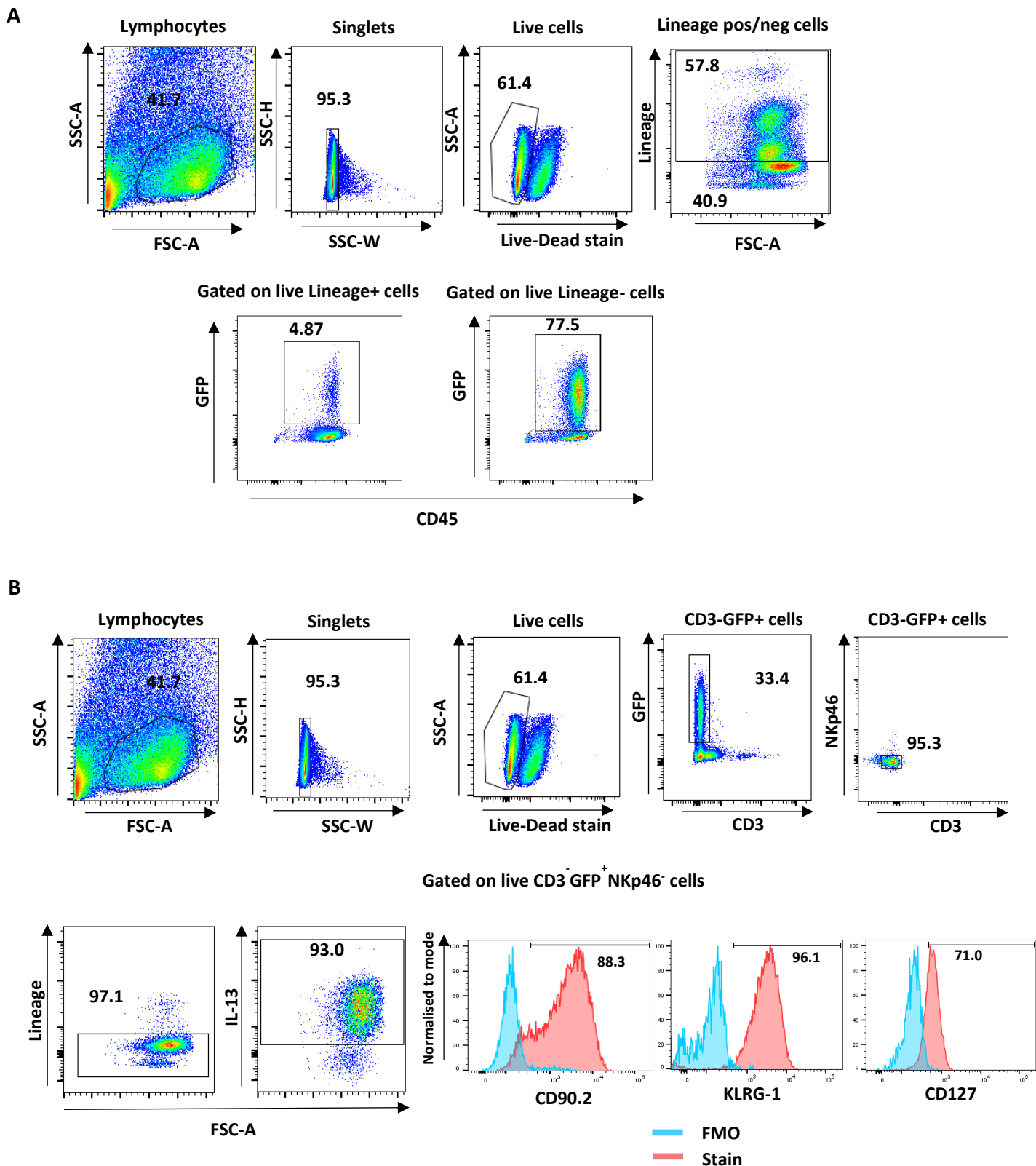
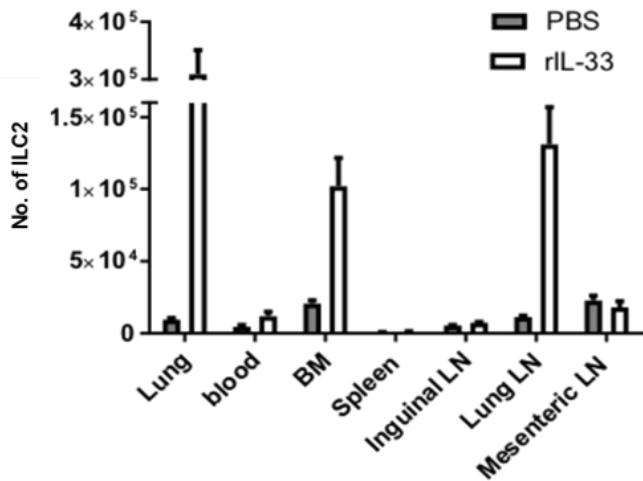


Figure 8





**Fig. S1. Gating strategy for identification of ILC2 populations, related to Fig. 1 A-C.** IL13-eGFP mice treated with 3 doses or rIL-33 (1 $\mu$ g per dose) over 1 week and culled 24h after the final dose. Cells were pre-gated on lymphoid, live (determined using a fixable live dead dye), lineage and frequencies of GFP<sup>+</sup>CD45<sup>+</sup> cells among lineage positive versus lineage negative cells was evaluated in (A). (B) ILC2 were defined by pre-gating on lymphoid, live (determined using a fixable live dead dye), GFP<sup>+</sup>CD3<sup>-</sup>NKp46<sup>-</sup> cells that were lineage (TCR $\beta$ , TCR $\gamma\delta$ , CD5, CD19, CD11b, CD11c, FC $\epsilon$ R1, GR-1, F4/80, and TER-119) negative cells and co-expressed intracellular IL-13 and surface expression of CD90.2, KLRG-1, CD127 as shown in histogram plots.



**Fig. S2. Quantification of ILC2 in different tissues, related to Fig. 1 A-C.** Il13-eGFP mice treated with 3 doses of rIL-33 (1  $\mu$ g per dose) or PBS (25  $\mu$ l) over 1 week and culled 24h after the final dose. ILC2 number in lungs, blood, bone marrow (BM), Spleen, Inguinal lymph node (LN), lung draining LN and mesenteric LN.  $n \geq 6$  mice per group. Data representative of 2 experiments.

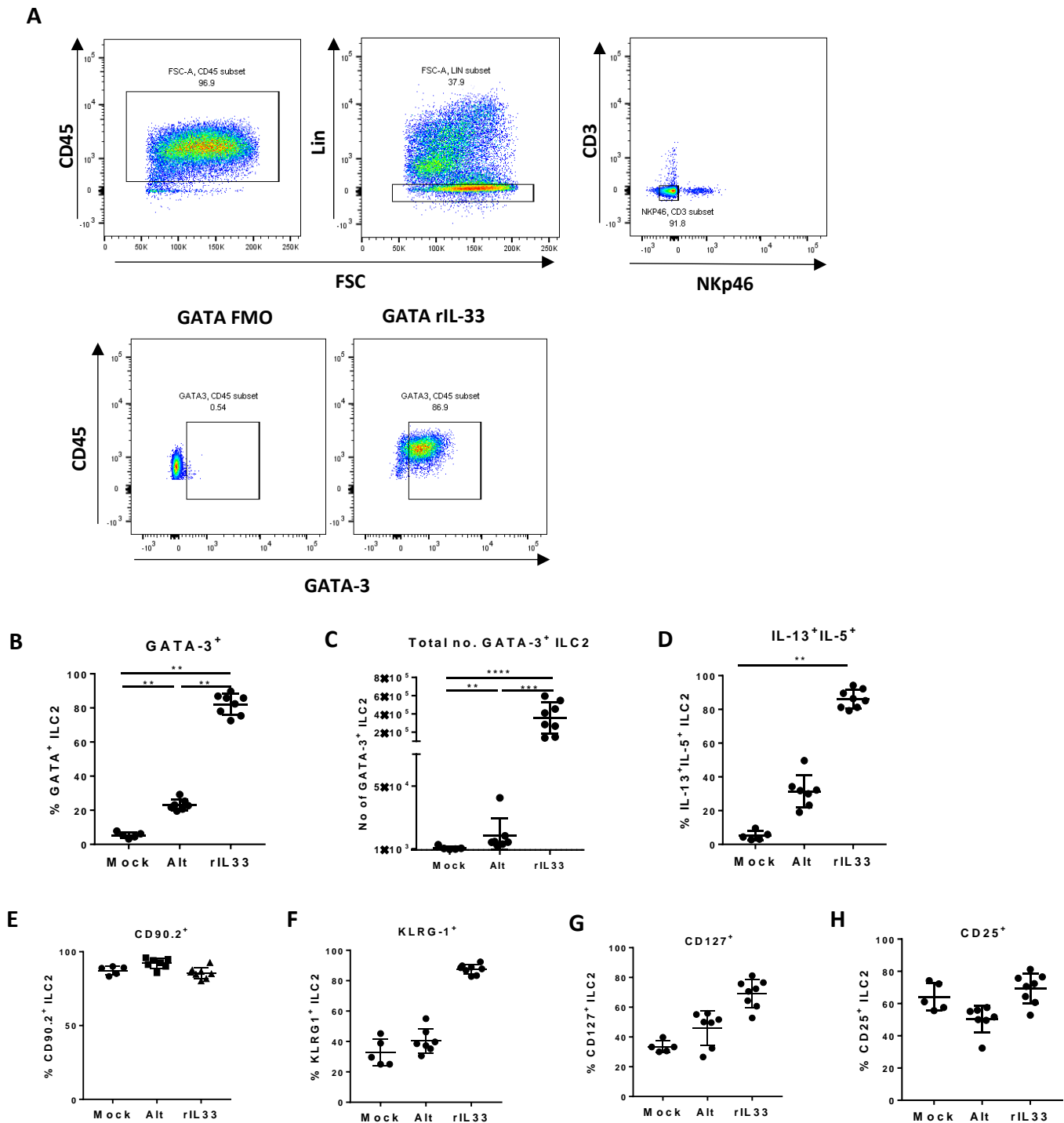


**Fig. S3. Gating strategy for identification of ILC2 populations based on GATA-3 expression, related to Fig. 1 A-C.** ILC2 were identified by gating on CD45<sup>+</sup> cells that were lineage neg (lin<sup>-</sup>) (Lineage cocktail: TCR $\beta$ , TCR $\gamma\delta$ , CD5, CD19, CD11b, CD11c, FC $\epsilon$ R1, GR-1, F4/80, and TER-119) lymphocytes that were additionally CD3<sup>-</sup> and NKp46<sup>-</sup> and expressed GATA-3 as shown in (A). (B) shows % of GATA-3<sup>+</sup> ILC2 in lungs of mock, Alt and IL-33 treated mice which were further quantified in number as shown in (C) and co-expressed IL-13 and IL-5 (D). ILC2 were further evaluated for percent expression of CD90.2 (E), KLRG-1(F), CD127 (G) and CD25 (H). Data shown for are from one of 4 independent experiments with a total of n  $\geq$  6 mice per group, \*  $P < 0.05$ , \*\*  $P < 0.01$ , \*\*\*  $P < 0.001$  and \*\*\*\*  $P < 0.0001$ .

**Fig. S4** Distribution of ILC2 and CD4 T cells in rIL-33 treated PCLS

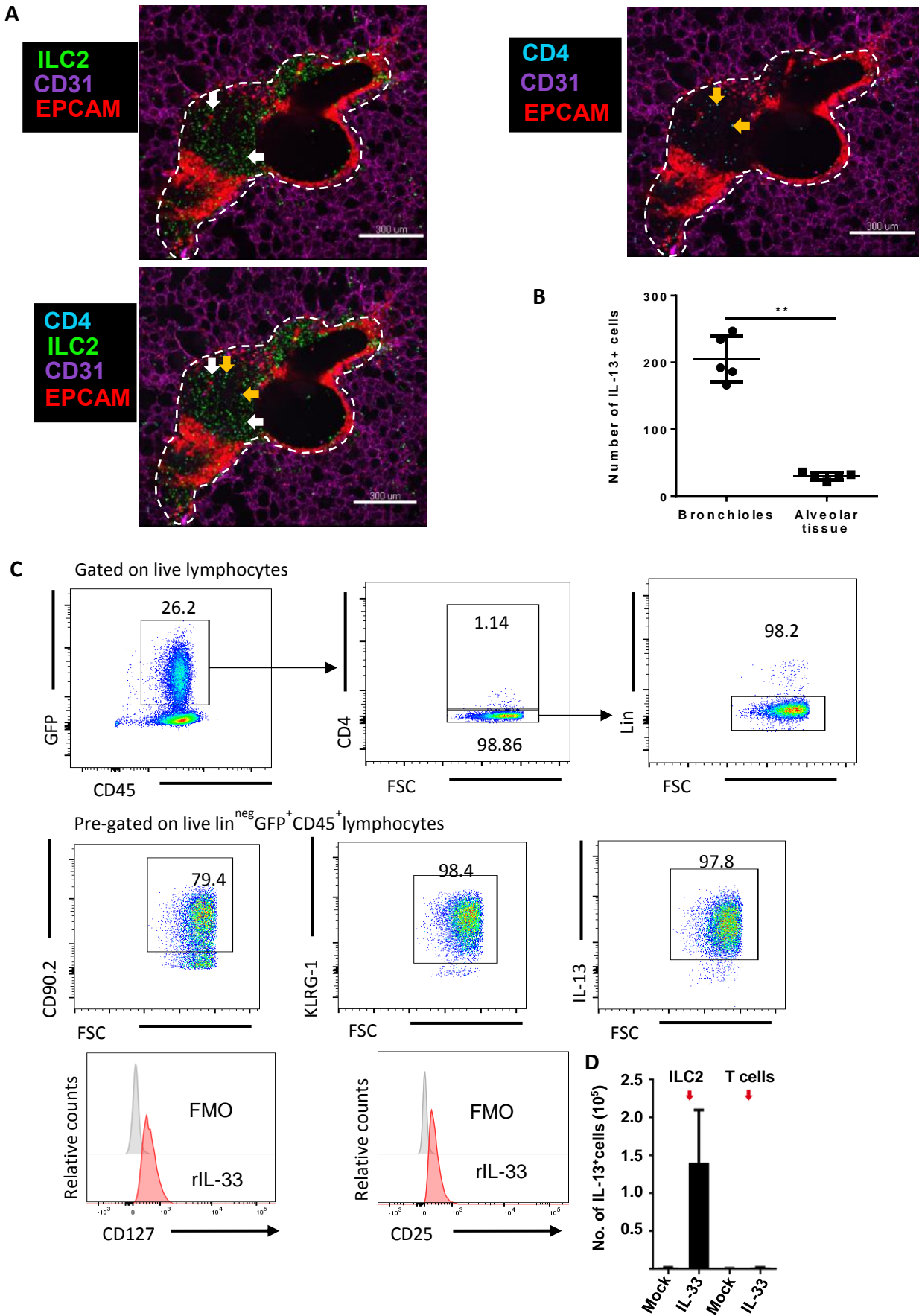


**Fig. S4. Distribution of ILC2 and CD4<sup>+</sup> T cells in rIL33 treated mice lungs, related to Fig. 1 D and F.** IL13-eGFP mice were treated with 3 doses of rIL-33 (1µg per dose), over 1 week and culled 24h after the final dose. **(A)** Live viable precision cut lung slices (PCLS) of 200µm thickness were obtained and stained for CD31 (Magenta, the lung structure and blood vessels), CD4 (cyan, T cells, orange arrow), EpCAM (Red, to visualise bronchial epithelium) and GFP (ILC2, white arrow). Highlighted in the insets (white dashed line) are areas of ILC2 and CD4<sup>+</sup> T cell accumulation. **(B)** Quantification of the number of IL-13<sup>+</sup>GFP<sup>+</sup> cells close to large blood vessels versus alveolar capillaries. **(C)** GFP<sup>+</sup> cells were assessed for ILC2 phenotypic expression by flow cytometry. Live GFP<sup>+</sup>CD45<sup>+</sup>CD4<sup>-</sup>Lin<sup>neg</sup> cells co-expressing CD90.2, KLRG-1 and intracellular IL-13 (dot plots), with CD127 and CD25 expression **depicted** as histogram plots. **(D)** Quantification of number of IL-13 producing ILC2 versus CD4 T cells. n = 4 mice per group. Data representative of 4 experiments. \*  $P < 0.05$ , **\*\*  $P < 0.01$** , \*\*\*  $P < 0.001$  and \*\*\*\*  $P < 0.0001$ .

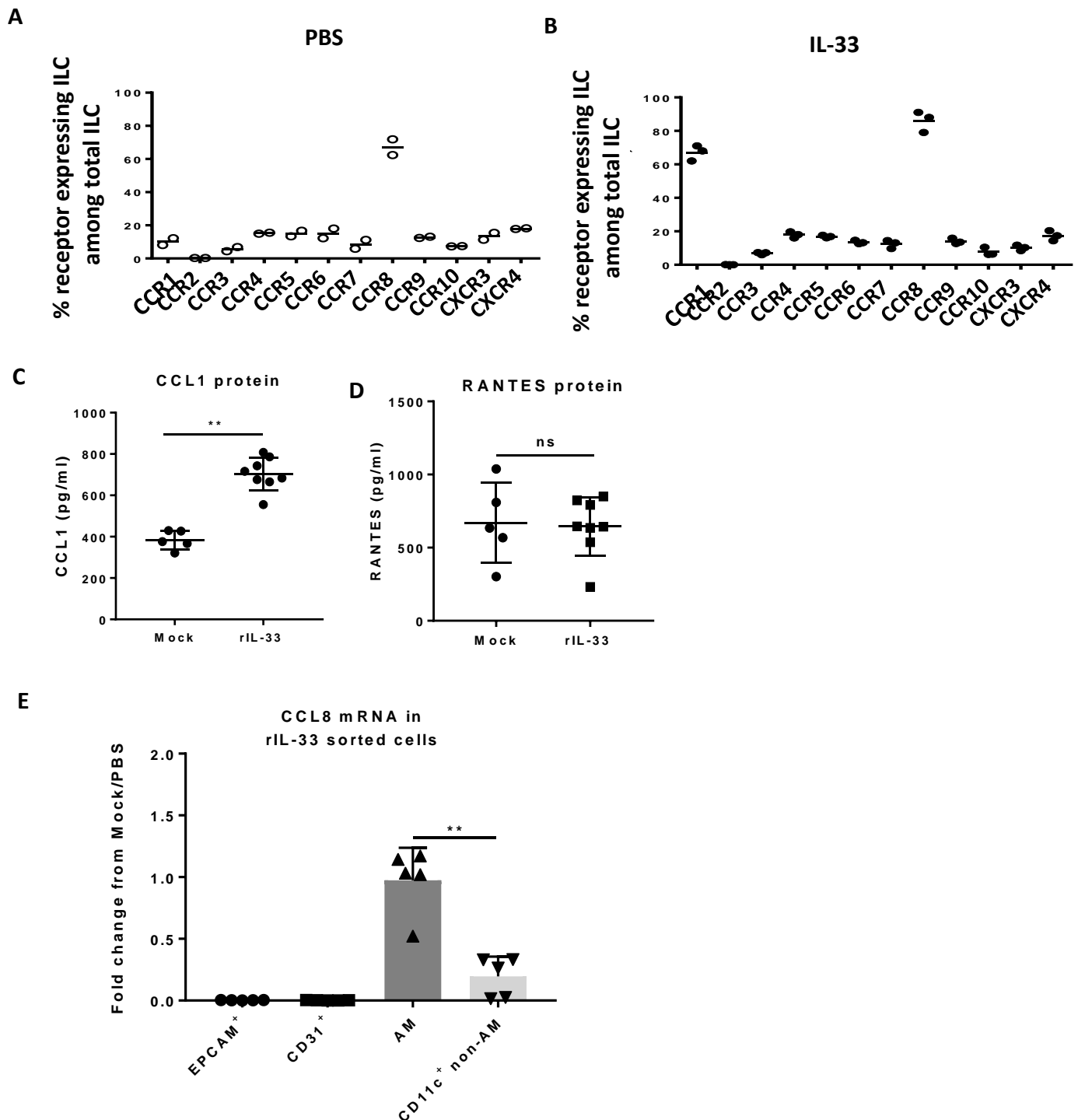


**Fig. S5. Chemokine receptor expression on ILC, related to Fig 4.** Mice were treated with rIL-33 (1 $\mu$ g, 3 times a week for 1 week) or PBS (25 $\mu$ l) and culled 24h after last dose. Percentage of lung ILC (GFP<sup>+</sup>CD45<sup>+</sup>Lin<sup>neg</sup>KLRG1<sup>+</sup>CD127<sup>+</sup>CD90.2<sup>+</sup>) expressing chemokine receptors in mice treated with **(A)** PBS or **(B)** rIL-33. Levels of **(C)** CCL1 **(D)** RANTES. **(E)** CCL8 expression levels in lung epithelial cells, endothelial cells, airway macrophages (AM) and non-AM. For panels A and B, n = 4 mice per group. Data representative of 4 experiments. For **C and D**, n = 5 mice (Mock(PBS)) and mice 6 mice (IL-33) per group and in **E**, n= 5 mice per group. Data representative of 2 experiments \* P < 0.05, **\*\* P < 0.01**, \*\*\* P < 0.001, \*\*\*\* P < 0.0001.



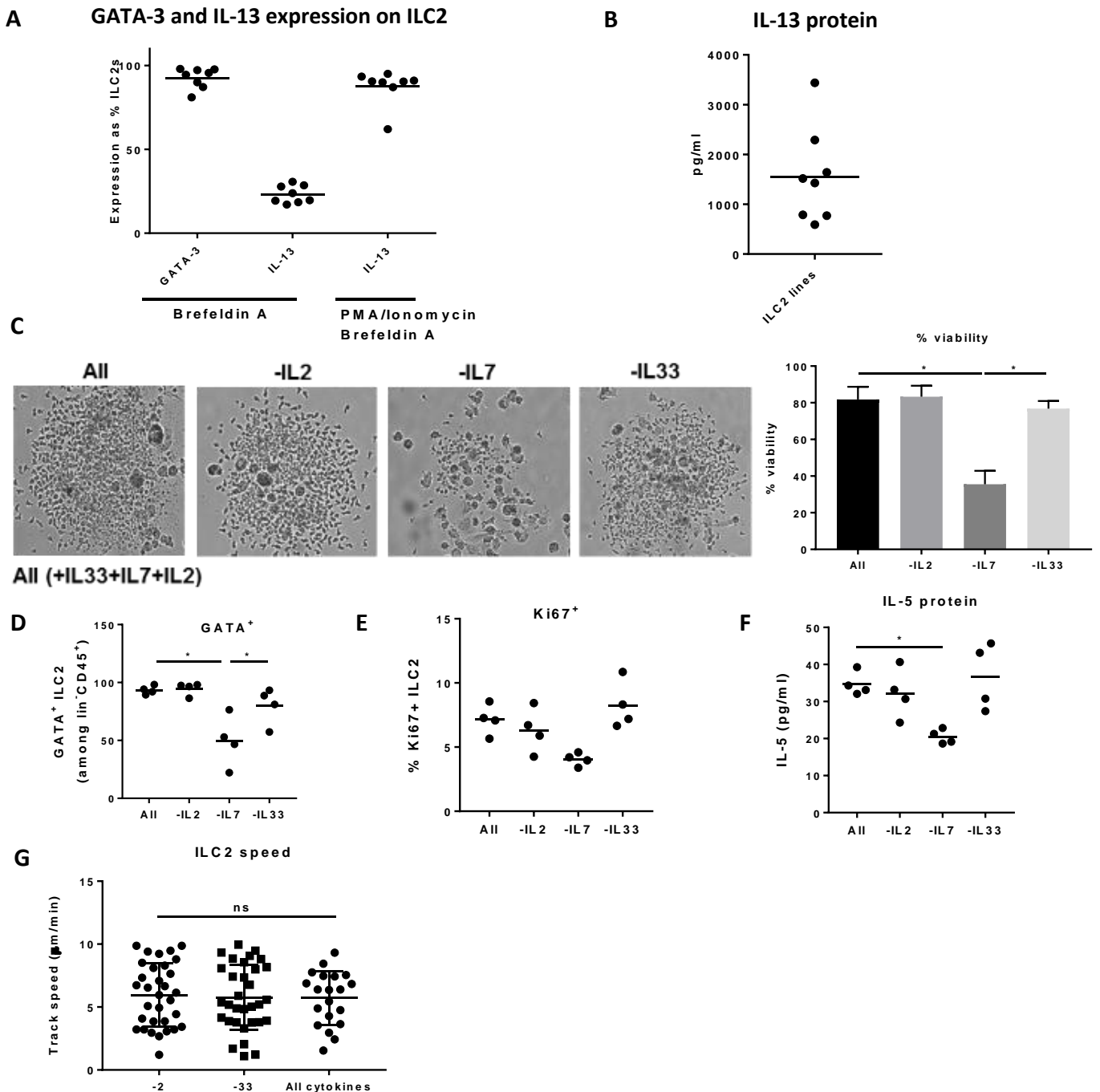


**Fig. S6. Phenotype and IL-13 production by human ILC2 lines, related to figure4 and 5.** Human ILC2 lines were generated. **(A)** GATA-3 and IL-13 expression by flow cytometry. **(B)** IL-13 production by ELISA as shown in. ILC2 lines were starved of either, IL-2, IL-7 or IL-33 for 72 hours and phenotype, proliferation, cytokine production and motility were compared to ILC2 that received all three cytokines. **(C)** Bright field images following starvation and quantification of viability. **(D)** GATA-3 and **(E)** Ki-67 expression assessed by flow cytometry. **(F)** IL-5 protein levels by ELISA. **(G)** track speed.  $n \geq 3$  donors (in triplicate). Data representative of 2 experiments.  $. *p < 0.05$ ,  $**p < 0.01$ ,  $***p < 0.001$  and,  $**** p < 0.0001$ .

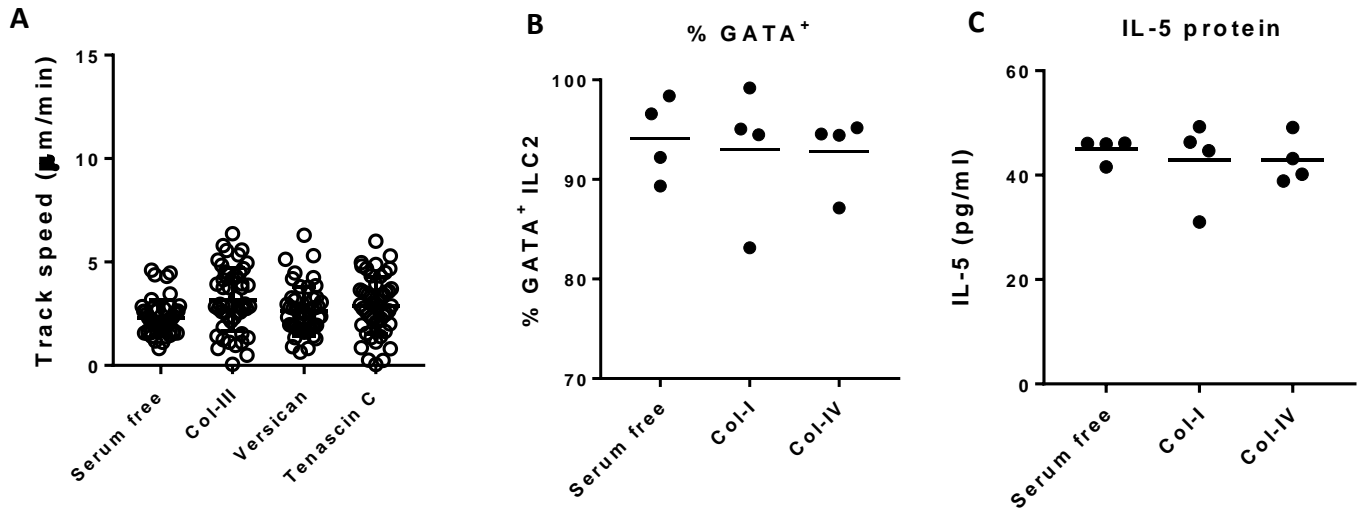


**Fig. S7. ILC2 motility on extracellular matrix proteins, collagen-III and proteoglycans Versican and tenascin-C, related to figure 5A-C. (A)** Human ILC2s seeded on tissue culture plates coated with either 10% FBS, collagen-III (col-III), versican or tenascin-C and migratory dynamics quantified as track speed. **(B)** GATA-3 expression and **(C)**IL-5 production from human ILC2 lines grown with either Collagen-I (col-I) or Collagen-IV (col-IV). Data shown are representative of 2 experiments with a total of n= 4 donor cell lines per treatment performed in triplicate.

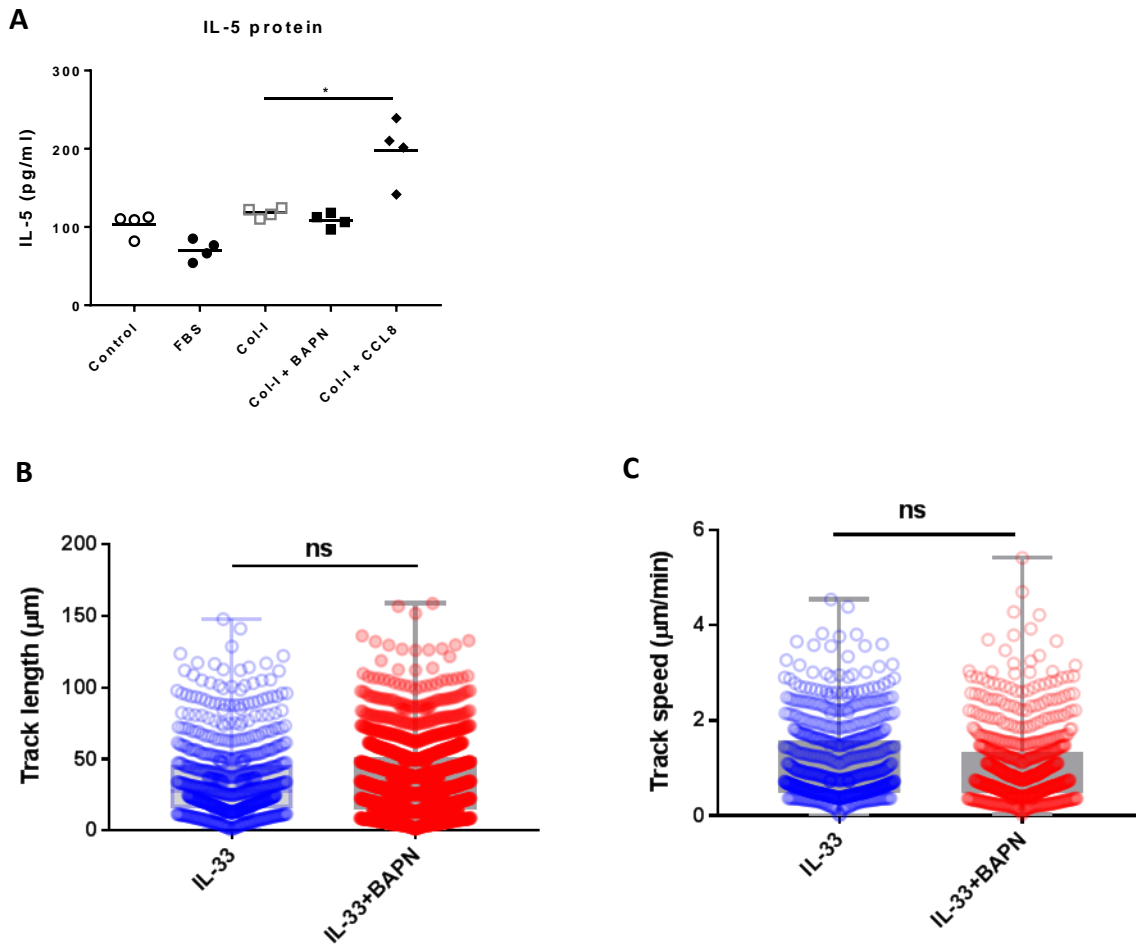


**Fig. S8. BAPN fails to affect ILC2 cytokine production and eosinophil movement, related to figure 8G.** Balb/c mice were treated with rIL-33 or PBS with or without BAPN. **(A)** Lung ILC2 were FACS sorted and seeded on FBS or collagen-I (col-I) in the presence or absence of BAPN or CCL8 and IL-5 production was assessed by ELISA. Live PCLS were obtained and imaged for eosinophils (Siglec-F<sup>+</sup>CD11c<sup>+</sup>) and motility was quantified by **(B)** track length and **(C)** track speed.  $n = 4$  mice per group. Data representative of 2 experiments.